Plasmons in Topological Systems

Dalton C. Hunley

Recommended Citation

Plasmons in Topological Systems

by

Dalton Hunley

Under the Direction of Vadym Apalkov, PhD

A Dissertation Submitted in Partial Fulfillment of the Requirements for the Degree of

Doctor of Philosophy

in the College of Arts and Sciences

Georgia State University

2023

ABSTRACT

Topological systems are not a recent development in physics, but the study of them has rapidly expanded in recent years due to advances in technology allowing for more accurate experimentation. This in return, has also led to more work for theoretical physicists to explore new possible applications of topological properties. Gaped graphene and transition metal dichalcogenides(TMDCs) are two examples of materials with topological properties due to symmetry points called valleys, where the dipole-transitions are most probable. This document contains two novel examples of those topological properties and their effects of surface plasmons. Firstly, we examine Chiral Berry Plasmons (CBP). CBP Modes have been shown to exist in 2D Dirac materials. These modes exist because of the role Berry Flux (net Berry curvature) plays in the materials themselves and are confined to the boundary in the absence of topological edge states. We show that in an optically pumped gaped graphene model, these CBP modes have an inherent tunability given by the temperature of the electrons in the system, the band gap of the material, and the relative populations created by the optical pumping of the system. Our calculations consider a quasi-equilibrium regime after thermalization but before relaxation, which occurs picoseconds later. In the other, we theoretically examine a TMDC Based Spaser Type II that has been optically pumped using an ultra-fast circularly-polarized pulse. The spasing system consists of a silver nanospheroid and a circular TMDC monolayer flake. The silver nanospheroid screens the incoming pulse and creates a nonuniform distribution of excitations in the TMDC valleys. As expected, these excitations still decay into localized surface plasmons (LSP) along the nanospheroid. However, valley polarization is only preserved in our system for small K-valley populations, as the required excited populations to contribute to the spasing "avalanche" are sometimes more significant than those that maintain valley polarization. The spaser also emits far-field radiation, shifting the polarization and magnifying the incoming pulse, showing promise in

that area of research.

INDEX WORDS: Near-field optics, Spaser, Optical pumping, Plasmonics, Symmetry protected topological states, Topological materials, Valleytronics, Chiral Berry Plasmons

Plasmons in Topological Systems

by

Dalton Hunley

Committee Chair:	Vadym Apalkov
Committee:	Brian Thoms
	Mukesh Dhamala
	Sidong Lei

Electronic Version Approved:

Office of Graduate Studies

College of Arts and Sciences

Georgia State University

May 2023

DEDICATION

To the one or two graduate students who will read this: I hope it helps.

TABLE OF CONTENTS

LIST OF FIGURES

CHAPTER 1

INTRODUCTION

1.1 Why Are We Doing This?

"Why is this important?" is a simple yet critical question we must answer as scientists. This is not necessarily a question posed to us by fellow researchers or the graduate students that continue our work when we are gone but by the general population of humanity to whom our research serves to benefit. The following dissertation consists of two critical projects composed over the past few years that may seem unrelated. However, both projects explore the theoretical possibilities of plasmons in topological systems. Why this is important is directly related to the nanoscale properties of plasmons, how topological properties give rise to non-reciprocity, and technology's constant journey towards the miniaturization of electronics.

A simple definition of plasmons is that they are the collective oscillations of electrons in metals.(6)(2) More importantly, a plasmon is a quasi-particle representative of the quantization of these oscillations. Plasmons are stimulated by external electromagnetic fields and interact strongly with them. Plasmons also act as bosons and obey Bose-Einstein statics, even though they consist of the oscillations of fermions. Since a minimum size does not restrict plasmons, they can exist at much smaller scales than photons. Why is this important? The size restriction of photons limits the possible applications of probing and sensing to objects above half a wavelength. However, a significant portion of the universe lies below this limit, such as subcellar structures and biological macromolecules below 10nm in size.(7)(8)

Recently, a new type of plasmon has been discovered that exhibits chiral properties, known as Chiral Berry Plasmons (CBPs). CBPs are collective oscillations of electrons in a metal characterized by a helical motion of the electron density. This helical motion results in the chiral nature of the CBPs, meaning that they exhibit different properties for left and right circularly polarized light. CBPs have unique properties, including a long propagation length, high confinement, and high sensitivity to changes in the surrounding environment.(9)

CBPs have potential applications in various fields, including sensing, optical communication, and quantum information processing. In sensing applications, CBPs can be used to detect changes in the refractive index of a material, making them useful for chemical and biological sensing. CBPs have also been shown to enhance the sensitivity of chiral spectroscopy techniques, which have potential applications in detecting chiral molecules and materials. In optical communication, CBPs can generate and manipulate light on the nanoscale, which has potential applications in developing nanoscale optical components such as couplers, filters, and switches. CBPs can also enhance the sensitivity of optical communication systems, making them useful for long-distance communication. CBPs have potential applications in quantum information processing in developing quantum communication systems. CBPs have been shown to exhibit strong coupling with quantum emitters such as quantum dots and single molecules, making them useful for the generation of entangled photons and quantum communication.(10)

Surface Plasmons can also be utilized to produce coherent radiation. When excited, surface plasmons can decay through various channels, including radiative decay, non-radiative

decay, and stimulated emission.(11) In a SPASER, a gain medium is placed near a metallic nanocavity, which supports surface plasmons. The gain medium is excited by an external light source, which causes the emission of surface plasmons. When the surface plasmons reach the metallic nanocavity, they undergo stimulated emission, resulting in the production of coherent radiation.(11)

SPASERs can revolutionize various fields, such as sensing, data storage and communication, and imaging. One of the most promising applications of SPASERs is sensing. SPASERs can detect small changes in a material's refractive index, making them attractive for applications in chemical and biological sensing. For example, SPASER-based biosensors have been demonstrated to detect single molecules, making them useful for the early detection of diseases and monitoring of biomolecules.(12)

Ref(8) goes explicitly into further detail on the applications of SPASERs as biological probes for the detection of cancerous cells. The importance of safely and accurately detecting potential cancers in biological systems should be evident to the reader. These properties will be crucial to Chapter 4, where plasmons are interchanged for photons in a potential nanoscale laser called a SPASER (Surface Plasmon Amplification by Stimulated Emission of Radiation).

In addition to medical applications, the nanoscale properties of plasmons allow for their use in data storage and communication with potential "on-chip" electronics. This is the unifying application to both projects in this dissertation. This area of nanoplasmonics requires us to dive into the topological properties of materials as well. Chapter 3 and Chapter 5

examine two different theoretical applications of plasmons to achieve the possible transfer of information on a nanoscale. Chapter 3 focuses on Chiral Berry Plasmons(CBPs), which act similarly to magnetoplasmons but without needing a magnetic field due to the nature of Berry Flux. This sidesteps the current complications in "on-chip" electronics that arise from the need for large magnetic fields at small scales.(9)(13) Why is this important? CBPs are topologically protected one-way transport systems with two possible directions. This allows nonmagnetic materials where CBPs exist to behave with non-reciprocity, similarly to the Integer Quantum Hall Effect and Topological Insulators.(**?**) This gives rise to the potential applications of CBPs in future Quantum Computers.(10) SPASERs, in Chapter 5, also have applications in "on-chip" electronics and future transistors below 10nm in size.(7) In this chapter, the spaser we examined was a Type II Topological spaser where a topological material acted as the gain medium for the system. The plasmons, in this case, do not directly arise on the topological material but are on the silver nanospheroid that is the active medium. The topological properties of the gain medium give rise to the stimulation of two distinct plasmonic modes. These modes could be potentially utilized for "on-chip" electronics.

This introduction has been brief and qualitative, but it should give the reader a decent background knowledge going into the theoretical summaries and new research in the remaining chapters about why we are doing this research. Nanoplasmonics is a field of research that has exploded in popularity since the turn of the millennium and promises to bring about radical technological advances that directly affect the common populace.

CHAPTER 2

THEORETICAL BACKGROUND

2.1 Plasmons

Plasmons are collective oscillations of the electrons present at the bulk and surface of conduct-ing materials and in the neighborhood of conducting particles.(14) They are quasi-particles similar to Phonons in mechanical vibrations. They follow Bose-Statistics as they are a col-lective motion of electron-hole pairs, leading to spin-1 quasi-particles.(6) Plasmons are the critical fundamental phenomena at the core of all research projects in this dissertation. Two distinct types of plasmons are studied here, bulk plasmons and surface plasmons. When exposed to an electromagnetic field, bulk plasmons are collective oscillations within a metal.
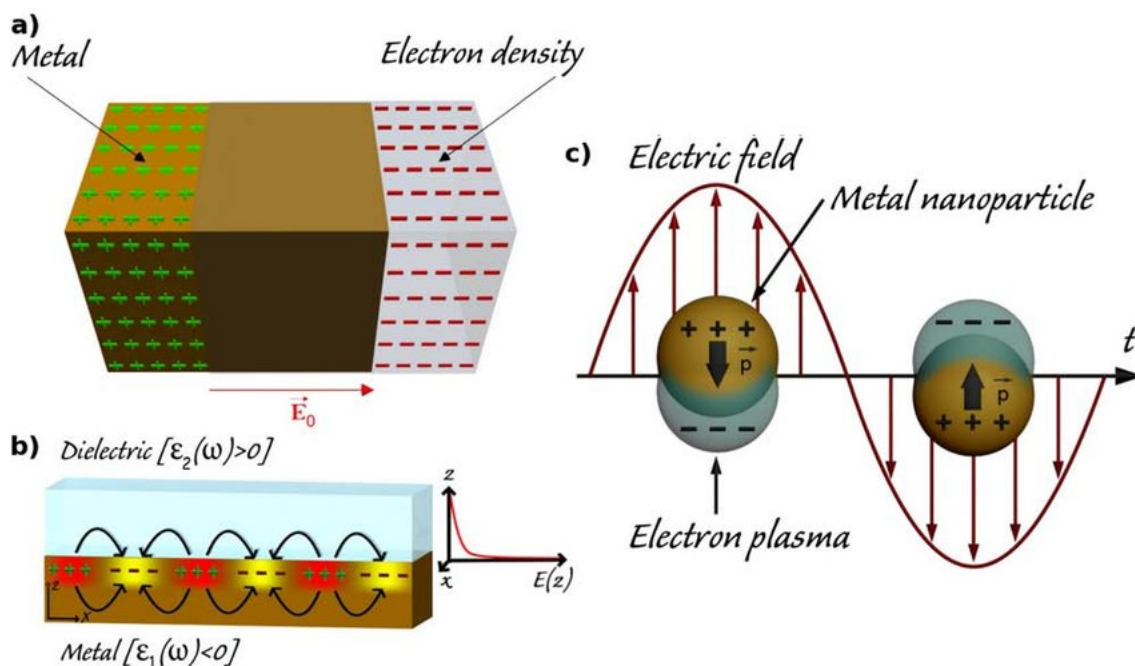
Figure 2.1 This figure is taken from Ref(1) and shows an artistic representation of Bulk plasmons (a), surface plasmons (b), and localized surface plasmons (c).

Surface plasmons are strongly confined to the surfaces of materials at an interface where one material has a positive dielectric constant, and another has a negative dielectric constant. They are well known and have already been extensively studied, but this paper will contain an essential derivation for completeness. The best place to start would be with Maxwell's Equations, as most textbooks begin with the macroscopic Maxwell equations to model electromagnetic response in materials.

2.1.1 Maxwell's Equations

$$\nabla \cdot \mathbf{D} = \rho_{ext} \tag{2.1}$$

$$\nabla \cdot \mathbf{B} = 0 \tag{2.2}$$

$$\nabla \times \mathbf{E} = -\frac{\partial \mathbf{B}}{\partial t} \tag{2.3}$$

$$\nabla \times \mathbf{H} = \mathbf{J}_{ext} + \frac{\partial \mathbf{D}}{\partial t} \tag{2.4}$$

These well-known equations connect the four macroscopic fields of electrodynamics. $\mathbf{D}$ is the dielectric displacement, $\mathbf{E}$ is the electric field, $\mathbf{H}$ is the magnetic field, and finally $\mathbf{B}$ is the magnetic induction. In addition, we have material-dependent relations in the limit of linear, isotropic, and non-magnetic media.(15)

$$\mathbf{D} = \epsilon_0 \epsilon \mathbf{E} \tag{2.5}$$

$$\mathbf{B} = \mu_0 \mathbf{H} \tag{2.6}$$

Next we have the dielectric susceptibility χ and a linear relationship between $\mathbf{P}$ and $\mathbf{E}$.(15)

$$\mathbf{P} = \epsilon_0 \chi \mathbf{E} \tag{2.7}$$

And finally, the current density:

$$\mathbf{J} = \sigma \mathbf{E} \tag{2.8}$$

2.1.2 Bulk Plasmons

Conceptually we can think of bulk plasmons through a "jello" model.(10) Imagine you have two sub-layers that make up your metal, one is a gelatinous structure of negative charge that is free to oscillate slightly, and the other is a solid fixed, solid, positively charged structure. The gelatinous structure is fixed atop the solid one and is electrically attracted to it. However, when exposed to an external electric field, the "jello" begins to "rock" back and forth. The "rocking" or the collective oscillations are known as bulk plasmons. We use the "plasma model" to derive bulk plasmons .(16) Effectively; we assume that an electron gas freely propagates near a background of positively charged ions. These free electrics oscillate around the ions when exposed to an external electromagnetic field. Suppose we imagine the electrons are harmonic oscillators in this situation. In that case, we can describe them as displaced from their equilibrium point relative to the positively charged ions, generating a

net polarization. The electric field, in this case, is:

$$\mathbf{D} = \epsilon_0 \mathbf{E} + \mathbf{P} \tag{2.9}$$

$$= \epsilon_0 \epsilon \mathbf{E} \tag{2.10}$$

Where ϵ is equal to:

$$\epsilon(\omega) = 1 - \frac{\omega_p^2}{\omega^2 + i\gamma\omega} \tag{2.11}$$

We can analyze equation 2.10 in two regimes. At low frequencies, metals become highly absorbing, and in this case, we can derive what is known as "skin depth," or the penetration depth of electromagnetic fields into the metal. At large frequencies, we can ignore any damping in the plasma, and then $\epsilon(\omega)$ is approximately real.

$$\epsilon(\omega) = 1 - \frac{\omega_p^2}{\omega^2} \tag{2.12}$$

Next, to characterize the propagation of the waves with this electric field, we need the dispersion relation:

$$\omega(k) = \sqrt{\omega_p^2 + \frac{k^2}{c^2}} \tag{2.13}$$

When $\omega = \omega_p$ and we are within the low-damping regime, a collective longitudinal oscillation mode exists parallel to the electric field. This mode is the jello rocking or, more scientifically,

Figure 2.2 This figure is taken from Ref(2) and shows an interface between a metal and dielectric.

the collective oscillation of the electron plasma above the fixed positive ion background. These are bulk plasmons.

2.1.3 Surface Plasmons

Surface Plasmons are conceptually similar to bulk plasmons, except they only exist along interfaces. Specifically interfaces between a metal and a dielectric medium. As stated above, the derivation for surface plasmons begins with Maxwell's equations. However, we introduce a boundary between two infinite planes at $x = 0$. One is metal, and the other is a dielectric. The transversal electric field components along the interface are(16):

$$D_{dz} = D_{mz} \tag{2.14}$$

$$E_{dx} = E_{mx} \tag{2.15}$$

$$E_{dy} = E_{my} \tag{2.16}$$

$$B_{dz} = B_{mz} \tag{2.17}$$

$$H_{dx} = H_{mx} \tag{2.18}$$

$$H_{dy} = H_{my} \tag{2.19}$$

Where d is the dielectric, and m is the metal. The resulting transverse-magnetic wave propagates along the x-axis as:

$$\mathbf{E}_i = (E_{ix}, 0, E_{iy}) \exp i(\mathbf{k_i} \cdot r - i\omega t) \tag{2.20}$$

$$\mathbf{H}_i = (0, H_{iy}, 0) \exp i(\mathbf{k} \cdot r - i\omega t) \tag{2.21}$$

$$\mathbf{D}_i = \epsilon_0 \epsilon_i \mathbf{E_i} \tag{2.22}$$

$$\mathbf{B}_i = \mu_0 \mathbf{H_i} \tag{2.23}$$

In this case, i is either, m or d. The wave vector $\mathbf{k}$ is $(k_x, 0, k_i z)$. When we plug these waves back into Maxwell's equations with zero charge and current densities, we can derive a relationship between the k_z components of the metal and dielectric. To ensure the modes are bound to the surface, we determine that k_z components must have opposites signs and

decay exponentially away from the surface.

$$\frac{k_{dz}}{\epsilon_d} = \frac{k_{mz}}{\epsilon_m} \qquad (2.24)$$

Looking at the derived relationship, though, the only way to achieve this is if the dielectrics themselves are of opposites signs, which is why surface plasmons can only exist at a boundary between a metal with a negative relative permittivity constant and a dielectric with a positive relative permittivity. This is because the penetration depth between the two materials is not equal. For example, in the dielectric, an electromagnetic wave penetrates to a distance of half a wavelength. However, in the metal, the oscillating electron plasma only exists down to the skin depth of the metal.

2.2 Berry Phase and Anomalous Phenomena Introduction

In addition to plasmons, another fundamental property of the projects in this dissertation is how they exploit the Berry phase of materials. The Berry phase arises in materials when eigenenergy states evolve adiabatically around a loop in parameter space.(17) The result of this loop is a phase gained by the eigenstate. Three fundamental properties of the Berry phase are important to our work.(18) The Berry phase is gauge invariant, unchanged up to a multiple of 2π, and is single-valued over the loop. Next, it is geometrical and can be expressed as a line integral over the loop. It can also be represented as an integral over a field or a surface on the loop. Finally, the Berry phase is analogous to other gauge field theories and differential geometries.(3)(19) helps us use it as a magnetic field in Chapter 3.

The field which the Berry phase is the integral over is known as the Berry curvature. So the Berry phase is analogous to the Aharonov-Bohm phase of a charged particle traversing a loop with a magnetic flux, and the Berry curvature is analogous to the magnetic field.(3)

Conceptually, we consider electrons as Bloch waves traveling through periodic potentials of a material's lattice structure. Where electrons behave as nearly free particles in response to external electromagnetic fields; however, this simple view does not explain all the effects of the electrons' response to the external field. In Chapter 3, we will explore an application of the "anomalous velocity" that arises from the incomplete view of electrons as nearly free particles. The anomalous velocity is an effect arising from the Berry curvature of the Bloch states of the material. Even in the absence of external fields, anomalous velocity exists.

Because of its importance to our research, this dissertation will contain a derivation of Berry phase and Berry curvature that follows the work of Xiao, Chang, and Niu (3) and will use the same notation.

2.2.1 Berry Effects from Adiabatic Evolution

We begin with a generic system described by a time-dependent Hamiltonian, which depends on a generic set of parameters, $\mathbf{R} = (R_1, R_2, ..)$

$$H = H(\mathbf{R}) \tag{2.25}$$

$$\mathbf{R} = \mathbf{R}(t) \tag{2.26}$$

$\mathbf{R}(t)$ evolves slowly along a path, as mentioned in the previous section. This path is labeled as C and exists inside the parameter space. Next, we can introduce a set of eigenstates for the Hamiltonian for each value of $\mathbf{R}(t)$ to form an orthonormal basis. This will allow us to apply the quantum adiabatic theorem as well.

$$H(\mathbf{R})|n(\mathbf{R})\rangle = E_n(\mathbf{R})|n(\mathbf{R})\rangle \tag{2.27}$$

We have yet to fully define $|n(\mathbf{R})\rangle$ here as an arbitrary phase can be applied to it without changing its physical definition. We can apply a gauge to the equation to remove the "arbitrary-ness" from the eigenstates. Xiao further details this in the appendix of Ref(3). Following the quantum adiabatic theorem, we can take the eigenstate of the system at $|n(\mathbf{R}(0))\rangle$ initially. As soon as the time evolution starts, the system will be in the instantaneous eigenstate $|n(\mathbf{R}(t))\rangle$.(20) This leaves us with one degree of freedom: the quantum state's phase.

$$|\psi_n(t)\rangle = \exp\left[i\gamma_n(t)\right]\exp\left[-\frac{i}{\hbar}\int_0^t E_n\mathbf{R}'(t')dt'\right]|n(\mathbf{R}(t))\rangle \tag{2.28}$$

Equation 2.28 may seem complicated, but it is the original time-dependent state with two-phase factors applied. Each exponent is a different phase factor, with the first exponent being the Berry phase we seek to derive and the second being the dynamical phase factor.(21) The dynamical phase factor is also well known, and it depends upon the energy of the system as it evolves and the time it takes the system to evolve. So, it is essential for the Adiabatic

Theorem of Quantum Mechanics. The Berry phase can also be expressed as the geometrical

phase, and it is independent of $\mathbf{R}$ and is not single-valued around the path.(22) So the total

phase an eigenstate gains as it evolves in time depends upon its energy and time and another

on the path it evolves through. Since equation 2.28 is just a time-dependent wave function,

we can use it within the time-dependent Schrodinger equation.

$$ i\hbar \frac{\partial}{\partial t} |\psi_n(t)\rangle = H(\mathbf{R}(t)) |\psi_n(t)\rangle \tag{2.29} $$

Next, we multiply both sides of the equation by $\langle n(\mathbf{R}(t))|$.

$$ \langle n(\mathbf{R}(t))| i\hbar \frac{\partial}{\partial t} |\psi_n(t)\rangle = \langle n(\mathbf{R}(t))| H(\mathbf{R}(t)) |\psi_n(t)\rangle \tag{2.30} $$

$$ \langle n(\mathbf{R}(t))| i\hbar \frac{\partial}{\partial t} (\exp\left[i\gamma_n(t)\right] \exp\left[-\frac{i}{\hbar} \int_0^t E_n \mathbf{R}'(t')dt'\right]) |n(\mathbf{R}(t))\rangle = \tag{2.31} $$

$$ \langle n(\mathbf{R}(t))| H(\mathbf{R}(t)) \exp\left[i\gamma_n(t)\right] \exp\left[-\frac{i}{\hbar} \int_0^t E_n \mathbf{R}'(t')dt'\right] |n(\mathbf{R}(t))\rangle $$

The dynamical phase cancels out, but the geometrical phase does not.

$$ \frac{\partial}{\partial t}\gamma_n(t) = i\langle n(\mathbf{R}(t))| \frac{\partial}{\partial \mathbf{R}} n(\mathbf{R}(t))\rangle \cdot \frac{\partial}{\partial t}\mathbf{R}(t) \tag{2.32} $$

This $\gamma_n(t)$ expression can also be expressed as a path integral in the parameter space.(3)

When the system completes its evolution through the whole path C in $\mathbf{R}$ its phase change

is:

$$|\psi_n(t)\rangle = \exp\left[i\gamma_n(C)\right] \exp\left[-\frac{i}{\hbar} \int_0^t E_n \mathbf{R}'(t')dt'\right]|\psi_n(0)\rangle \tag{2.33}$$

Thus giving us the result for the geometric phase:

$$\gamma_n(C) = i \int_C \langle n(\mathbf{R})| \frac{\partial}{\partial \mathbf{R}} n(\mathbf{R})\rangle \cdot d\mathbf{R} \tag{2.34}$$

The normalization factor on $\langle n(\mathbf{R})|\frac{\partial}{\partial \mathbf{R}} n(\mathbf{R})\rangle$ is imaginary, which gives us a real result for the geometric phase as well.(22) Now that we have the geometric phase or Berry's phase, we have this interesting vector-valued function that it depends on:

$$A_n(\mathbf{R}) = i\langle n(\mathbf{R})| \frac{\partial}{\partial \mathbf{R}} n(\mathbf{R})\rangle \tag{2.35}$$

We have defined this as $A_n(\mathbf{R})$, which is the Berry connection or the Berry vector potential.(17) So, a more general form for the Berry phase is:

$$\gamma_n(C) = \int_C A_n(\mathbf{R}) \cdot d\mathbf{R} \tag{2.36}$$

Michael Berry also proved that even though this vector potential was gauge-dependent if taken around a closed path, the gauge transformation is single-valued.(22) With the transformation from $\mathbf{R}(0)$ to $\mathbf{R}(C)$ being $2\pi\times$ some integer. It also cannot be removed from the equation. Therefore, after the effects of all of the above, γ_n becomes gauge-invariant.(3)

Solving for γ_n can be awkward because of the single-valued basis requirements on our basis of the parameter space. However, we know from Stokes's Theorem that an integral over a closed loop or path can be expressed as an integral over a surface, with the path defining the boundaries of the surface.

$$\gamma_n = \int_C A_n(\mathbf{R}) \cdot d\mathbf{R} = \int \int_C \nabla \times A_n(\mathbf{R}) \cdot d\mathbf{S} \qquad (2.37)$$

Next we define $\nabla \times A_n(\mathbf{R})$ as $\mathbf{\Omega}_n(\mathbf{R})$.

$$\gamma_n = \int_\mathbf{S} \mathbf{\Omega}_n(\mathbf{R}) \cdot d\mathbf{S} \qquad (2.38)$$

$\mathbf{\Omega}_n(\mathbf{R})$ is known as the Berry curvature. Since the adiabatic approximation is a projection operation, we can view the Berry curvature as the "residual" interaction of the projected-out energy levels.(3) There is also a local conservation law for Berry curvature that states that when all energy levels are considered, the total Berry curvature vanishes for each value of the parameter space along the loop. This is a general theoretical description of Berry curvature; however, in this dissertation, we are specifically interested in how Berry curvature manifests itself in physical systems. The Berry curvature is an intrinsic property in Bloch bands because it only depends on the wave function. The band structure of some specific materials also has nonzero Berry curvature and breaks the local conservation law mentioned above. Specially, these materials are crystalline solids with broken $\mathscr{T}$ symmetry or inversion symmetry. When these materials have an external electric field applied, a linear variation in
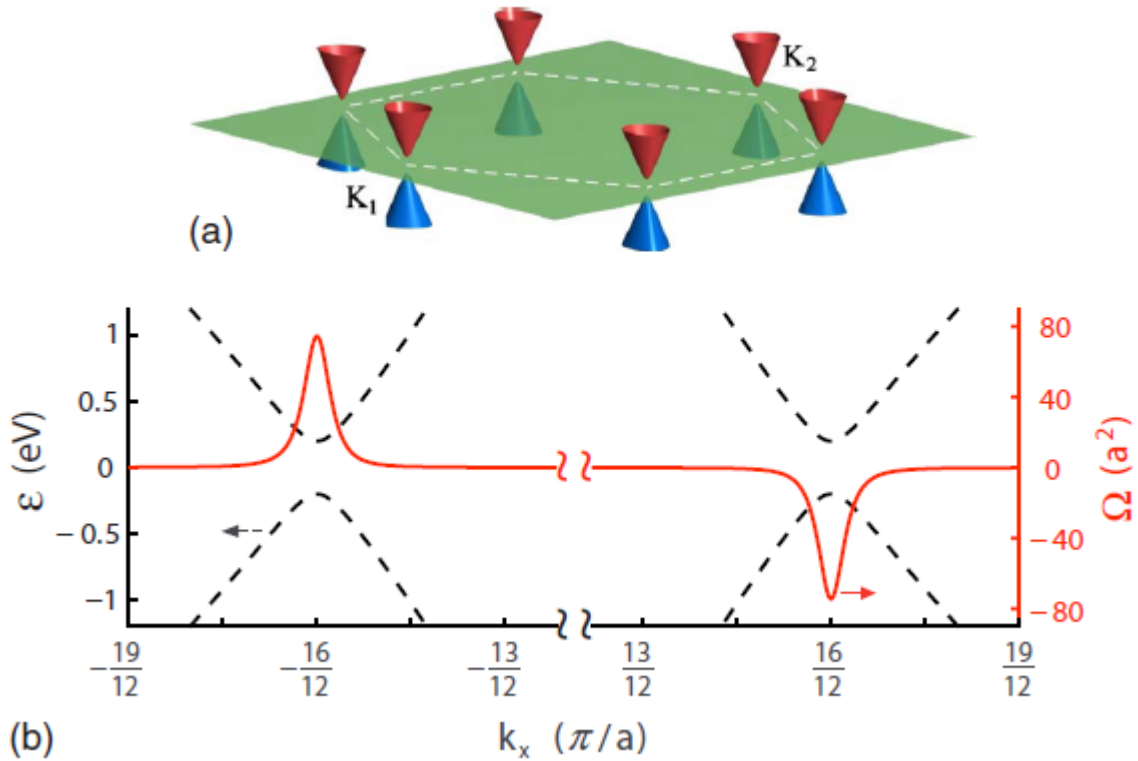
Figure 2.3 This image is taken from Ref(3) and shows the energy bands (2.2.a) and Berry curvature (2.2.b) of a 2D crystalline structure. The dashed lines are the K and K' valley's respectively and the solid red line shows the magnitude of Berry curvature inside each valley.

the crystal momentum $\mathbf{q}$ is initiated. $\mathbf{q}$ then covers the entire Brillouin zone of the crystal, which creates a closed path loop. The topology of this structure is that of a torus where two different points, $\mathbf{q}$ and $\mathbf{q} + \mathbf{G}$, are overlapping and the same. Here, $\mathbf{G}$ is the reciprocal lattice vector.(3)

To derive these effects, we must start with Bloch's Theorem. Bloch's Theorem describes solids as periodic potentials. Using the independent electron approximation, the appropriate

Hamiltonian for an electron in this system is:

$$H = \frac{\hat{p}^2}{2m} + V(\mathbf{r}) \tag{2.39}$$

$V(\mathbf{r})$ represents the periodic potential of the crystalline solid, $V(\mathbf{r}) = V(\mathbf{r} + \mathbf{a})$. The eigenstates of this Hamiltonian have the following form:

$$\psi_{n\mathbf{q}}(\mathbf{r} + \mathbf{a}) = e^{i\mathbf{q}\cdot\mathbf{a}}\psi_{n\mathbf{q}}(\mathbf{r}) \tag{2.40}$$

To make sure we have a $\mathbf{q}$-dependent Hamiltonian to match our $\mathbf{q}$-dependent, we just apply a unitary transformation:

$$H(\mathbf{q}) = e^{-i\mathbf{q}\cdot\mathbf{r}}He^{i\mathbf{q}\cdot\mathbf{r}} = \frac{(p + \hat{\hbar\mathbf{q}})^2}{2m} + V(\mathbf{r}) \tag{2.41}$$

Now, if $\mathbf{q}$ varies in momentum space, then our new Bloch states will acquire a Berry phase:

$$\gamma_n = \int_C \langle u_n(\mathbf{q})|i\nabla_\mathbf{q}|u_n(\mathbf{q})\rangle d\mathbf{q} \tag{2.42}$$

Where $u_n(\mathbf{q})$ is the momentum space variant of the transformed eigenstate $u_{n\mathbf{q}}(\mathbf{r}) = e^{i\mathbf{q}\cdot\mathbf{a}}\psi_{n\mathbf{q}}(\mathbf{r})$. Following the theoretical approach outlined earlier in this subsection, we arrive at an equation for the Berry curvature:

$$\Omega_n(\mathbf{q}) = \nabla_\mathbf{q} \times \langle u_n(\mathbf{q})|i\nabla_\mathbf{q}|u_n(\mathbf{q})\rangle \tag{2.43}$$
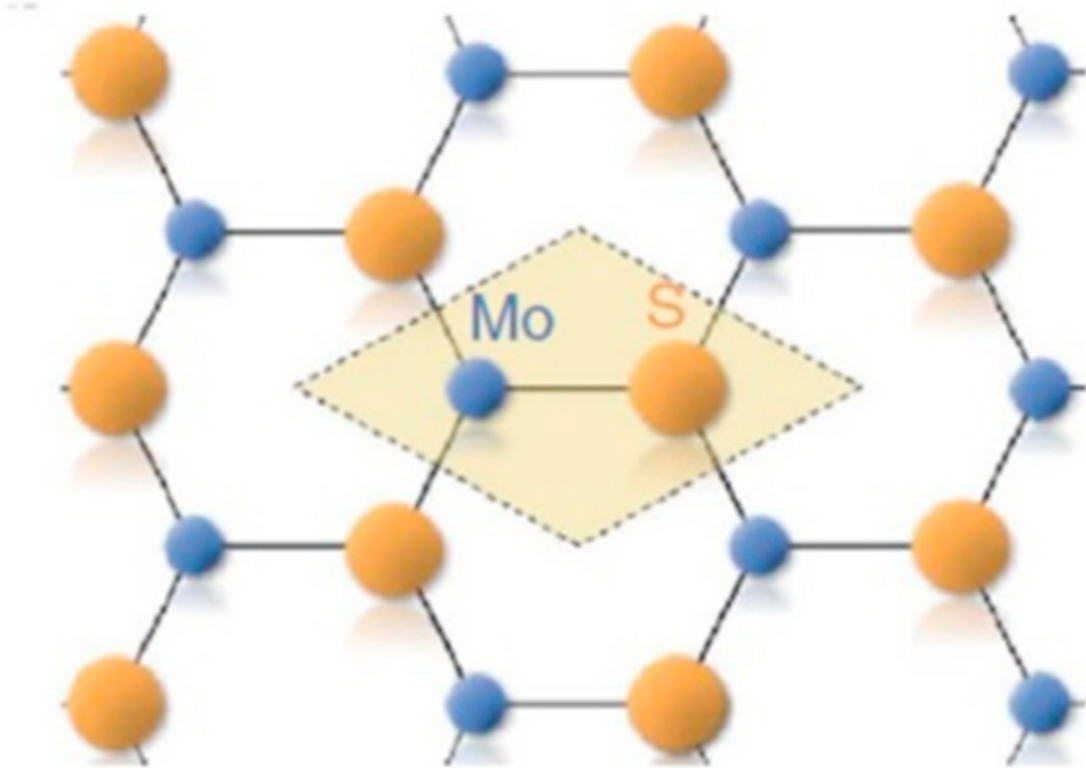
Figure 2.4 This image is taken from Ref(4) and is the crystalline structure of MoS_2. A TMDC with a hexagonal structure made up of Mo atoms (blue) and S atoms (yellow).

We will apply this formalism to gaped graphene and transition metal dichalcogenide (TMDC) monolayers in our projects.

2.3 Transition metal dichalcogenide monolayers

Transition metal dichalcogenide (TMDC) monolayers have emerged as a promising class of two-dimensional materials with unique electronic and optical properties. These materials are composed of transition metal atoms, such as molybdenum (Mo) or tungsten (W), which are sandwiched between two layers of chalcogen atoms, such as sulfur (S) or selenium

(Se).(23)(24) The resulting structure is a flat, atomically thin layer that can be as thin as a single atomic layer.

TMDC monolayers have attracted significant attention due to their exciting properties, such as high electron mobility, strong light-matter interactions, and considerable excitonic binding energies, making them potential candidates for applications in electronics, optoelectronics, and photonics. For example, TMDC monolayers have been demonstrated to exhibit high photoresponsivity and photoconductivity, making them promising materials for photodetectors and solar cells. Additionally, TMDC monolayers have been shown to have strong non-linear optical properties, which make them attractive for applications in ultrafast optical switching and frequency conversion.(23)(24)

The unique properties of TMDC monolayers can be attributed to their two-dimensional structure, which leads to quantum confinement effects and strong interatomic interactions within the layer. The properties of TMDC monolayers can also be tuned by varying the composition and structure of the material, making it possible to design materials with tailored properties.(23)(24)

The study of TMDC monolayers is an active area of research, with numerous studies focusing on these materials' synthesis, characterization, and applications. Researchers continue exploring the potential of TMDC monolayers in various applications, including electronic and optoelectronic devices, energy storage and conversion, and sensing.(23)(24)
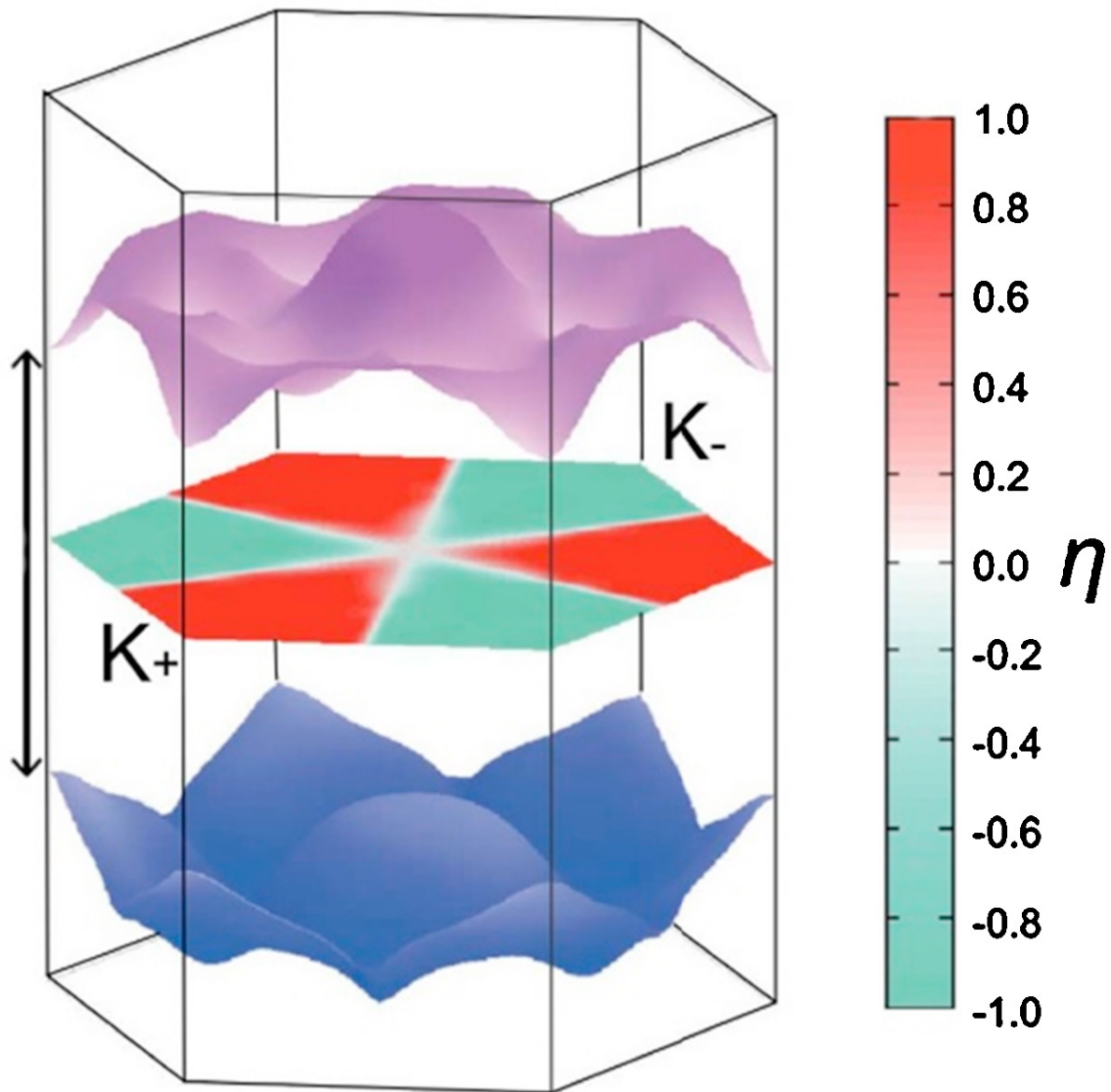
Figure 2.5 This image is also from Ref(4). It shows the 3-dimensional energy band structure of MoS_2. The purple layer is the conduction band and the blue layer represents the valence band. The central layer is color coordinated to show the difference in polarization from the K and K' valleys.

CHAPTER 3
CHIRAL BERRY PLASMONS

3.1 Introduction

Recently chiral Berry plasmons without magnetic fields have been theoretically proposed.(13)(9) These plasmonic systems are analogous to well established research in magnetoplasmons that has been conducted for nearly forty years now.(25)(26) The key relation between the two arises from the properties of Bloch band Berry curvature.(27) Berry curvature is a topological property of materials that acts as a magnetic field in momentum space. This property of the system creates an environment that could produce on-chip technological systems without the need for strong external fields.

Magnetoplasmons have edge modes arise in the presence of a magnetic field.(26) Their frequency is proportional to B^{-1} To summarize, the applied magnetic field introduces a transverse component on the electrons via the Lorentz Force. The trajectory of free electrons becomes elliptical in the plane of the metal perpendicular to B. This motion is nearly circular.(28) Along the boundary of the material these modes lead to one-way propagation.

Previous work has shown that nonmagnetic materials are capable of supporting chiral Berry plasmons. These materials include gaped graphene and monolayer transition dichalcogenides (TMDC). In equilibrium, these materials have two valleys at the K and K' points with opposite Berry curvature and protected by time reversal symmetry, or $\mathscr{T}$-symmetry.(29) This leads to a net Berry flux($\mathscr{F}$) of 0 in the system. However, out of equilibrium it is possible to create an imbalance in the populations of the K and K' valleys and break $\mathscr{T}$-symmetry.

One way to achieve an imbalance in the K and K' valley populations is through optical pumping leading to valley polarization. Valley polarization generated by a circularly polarized applied electric field has been extensively explored prior to this paper.(29) Including how it generates chiral Berry plasmons.(13)(9) In summary, the nonzero Berry flux gives rise to an anomalous velocity transverse to the applied electric field. The mathematical derivation of the anomalous velocity effects are shown in Ref(13), Ref(3), and summarized later in this paper. This leads to a net nonzero Berry flux and to anomalous Hall-like effects.(13)(9)

However, in previous work, only one of the chiral Berry plasmon edge modes was protected for large values of q. This is because the edge mode splitting was determined by the wave vector q and the Berry Flux, $\hbar\Delta\omega \approx Const. \times q\mathscr{F}$.(13) Therefore, as the wave vector increases, the splitting increases until the positive edge mode uncouples from the edge of the material and merges with the bulk frequency.(13) Fascinatingly, this is not unique to chiral plasmons without a magnetic field but is also analogous to 2D edge magneotoplasmons. As for certain values of magnetic field the positive edge mode is indistinguishable from the bulk.(26)

The goal of this chapter is to theoretically examine possible ways to modify the plasmon edge modes that arise due to the presence of nonzero Berry flux in order to find what external conditions lead to the largest range of q values that two edge modes exist and are both distinguishable from the bulk mode. Magnetoplasmon edge mode splittings are determined by the cyclotron frequency which depends on the incoming magnetic field strength. However, Berry plasmons are determined by the plasmon wavelength and Berry flux. Selecting

appropriate plasmon wave lengths was discussed in Ref(9), therefore here we will discuss controlling the Berry plasmon edge mode splittings by modifying the Berry flux. We show that modifications to: the material's band gap, the Fermi level at which the valleys are populated, and the temperature the material is held at all have profound effects on the existence of the edge modes.

3.2 Mathematical Methods

3.2.1 Kubo Formula and Conductivity

The Plasmon modes for this project were found in a similar method to Song et al, in Ref(13) as they proposed an alternative method involving the conductivity matrix. This allows us to better explore the effects of Berry Flux on the system. We use the Euler equations for electron density while working in terms of Fourier modes ($\rho(\mathbf{r}, t) = \rho_\omega(\mathbf{r})e^{i\omega t}$, $\mathbf{j}(\mathbf{r}, t) = \mathbf{j}_\omega(\mathbf{r})e^{i\omega t}$, and $\phi(\mathbf{r}, t) = \phi_\omega(\mathbf{r})e^{i\omega t}$)

$$i\omega \rho_\omega(\mathbf{r}) + \nabla \cdot \mathbf{j}_\omega(\mathbf{r}) = 0 \tag{3.1}$$

$$\mathbf{j}_\omega(\mathbf{r}) = \sigma_{ij}(\omega)\nabla \phi_\omega(\mathbf{r}) \tag{3.2}$$

Here, $\phi_\omega(\mathbf{r})$ is the electric potential, $\mathbf{j}_\omega(\mathbf{r})$ is the current density, $\rho_\omega(\mathbf{r})$ is the charge density, and $\sigma_{ij}(\omega)$ is the conductivity matrix. For calculating $\sigma_{ij}(\omega)$ we used the Kubo formula. The conductivity from the Kubo Formula is:

$$\sigma_{ij}(q,\omega) = \frac{i\hbar g}{4\pi^2} \int d\mathbf{k} \sum_{m,n} \frac{f_n(\mathbf{k}) - f_m(\mathbf{k}+\mathbf{q})}{E_m(\mathbf{k}+\mathbf{q}) - E_n(\mathbf{k})} \tag{3.3}$$

$$\times \frac{\langle n,\mathbf{k}|\hat{j}_i|m,\mathbf{k}+\mathbf{q}\rangle\langle m,\mathbf{k}+\mathbf{q}|\hat{j}_j|n,\mathbf{k}\rangle}{\hbar\omega + i0^+ - E_m(\mathbf{k}+\mathbf{q}) + E_n(\mathbf{k})}$$

Where $f_n(\mathbf{k})$ is the Fermi-Dirac distribution and g is the degeneracy of the electrons. For example, in the case of graphene, $g = g_s g_v$ g_s is the spin degeneracy and g_v is the valley degeneracy. The current operators are defined by $\hat{j} = e\hat{v}$ and $\hat{v} = \frac{i}{\hbar}[\mathbf{r}, H]$. The summation is over the band indices m and n. We summarize Eq.(3) as:

$$\sigma_{ij}(q,\omega) = \frac{i\hbar g}{4\pi^2} \int d\mathbf{k} \sum_{m,n} \frac{\Delta f_{nm}}{\Delta E_{mn}} \times \frac{M_{mn}^{ij}}{\hbar\omega + i0^+ - \Delta E_{mn}} \tag{3.4}$$

$$\Delta f_{nm} = f_n(\mathbf{k}) - f_m(\mathbf{k}+\mathbf{q}) \tag{3.5}$$

$$\Delta E_{mn} = E_m(\mathbf{k}+\mathbf{q}) - E_n(\mathbf{k}) \tag{3.6}$$

$$M_{mn}^{ij} = \langle n,\mathbf{k}|\hat{j}_i|m,\mathbf{k}+\mathbf{q}\rangle\langle m,\mathbf{k}+\mathbf{q}|\hat{j}_j|n,\mathbf{k}\rangle \tag{3.7}$$

From here we are able to examine the intra-band and inter-band conductivity using a small q and ω approximation. The intraband-conductivity is given by setting $m = n = \alpha$

$$\sigma_{ij}^{\text{intra},\alpha}(q,\omega) = \frac{i\hbar g}{4\pi^2} \int d\mathbf{k} \frac{\Delta f_{\alpha\alpha}}{\Delta E_{\alpha\alpha}} \times \frac{M_{\alpha\alpha}^{ij}}{\hbar\omega + i0^+ - \Delta E_{\alpha\alpha}} \tag{3.8}$$

$$= \frac{i\hbar g}{4\pi^2} \left\{ \int d\mathbf{k} \frac{\Delta f_{\alpha\alpha}}{\Delta E_{\alpha\alpha}} \times \frac{M_{\alpha\alpha}^{ij}}{\hbar\omega - \Delta E_{\alpha\alpha}} + \int d\mathbf{k} \frac{\Delta f_{\alpha\alpha}}{\Delta E_{\alpha\alpha}} \times M_{\alpha\alpha}^{ij} \times [-i\pi\delta(\hbar\omega - \Delta E_{\alpha\alpha})] \right\} \tag{3.9}$$

or

$$\Im m[\sigma_{ij}^{\text{intra},\alpha}(q,\omega)] = \frac{i\hbar g}{4\pi^2}\left\{\int d\mathbf{k}\frac{\Delta f_{\alpha\alpha}}{\Delta E_{\alpha\alpha}}\times\frac{M_{\alpha\alpha}^{ij}}{\hbar\omega-\Delta E_{\alpha\alpha}}\right\} \tag{3.10}$$

$$\Re e[\sigma_{ij}^{\text{intra},\alpha}(q,\omega)] = \frac{i\hbar g}{4\pi^2}\left\{\int d\mathbf{k}\frac{\Delta f_{\alpha\alpha}}{\Delta E_{\alpha\alpha}}\times M_{\alpha\alpha}^{ij}\times[-i\pi\delta(\hbar\omega-\Delta E_{\alpha\alpha})]\right\}$$

The matrix element $M_{\alpha\alpha}$ is:

$$M_{\alpha\alpha}^{ij} = e^2\langle\alpha,\mathbf{k}|\frac{\partial H}{\hbar\partial k_i}|\alpha,\mathbf{k}+\mathbf{q}\rangle\langle\alpha,\mathbf{k}+\mathbf{q}|\frac{\partial H}{\hbar\partial k_j}|\alpha,\mathbf{k}\rangle, \tag{3.11}$$

In the case of the inter-band conductivity, we assume $\Delta E_{mn}\gg\hbar\omega\gg\hbar v_F q$ and obtain a description of the topological properties of the system. Eq.(4.4) becomes:

$$\sigma_{ij}^{\text{inter}}(q,\omega)\simeq\frac{i\hbar g}{8\pi^2}\int d\mathbf{k}\sum_n\sum_{m\neq n}\frac{\Delta f_{nm}\left(M_{mn}^{ij}-M_{mn}^{ij*}\right)}{-\Delta E_{mn}^2} \tag{3.12}$$

$$\sigma_{ij}^{\text{inter}}(q,\omega)\simeq\begin{cases}0, & i=j\\[2ex]\frac{-e^2 g}{4\pi^2\hbar}\int d\mathbf{k}\sum_n, f(E_n(\mathbf{k}))\Omega_n^{ij}(\mathbf{k}), & i\neq j\end{cases} \tag{3.13}$$

$$\Omega_n^{ij}(\mathbf{k}) = i\sum_{m\neq n}\frac{\langle n,\mathbf{k}|\hat{j}_i|m,\mathbf{k}\rangle\langle m,\mathbf{k}|\hat{j}_j|n,\mathbf{k}\rangle-h.c.}{\Delta E_{mn}^2} \tag{3.14}$$

Eq.(4.14) is the Berry Curvature of the system written as a summation of eigenstates that arises naturally within the Kubo formula.(3)

Here is a quick derivation of Eq. 4.12-14:

$$\sigma_{ij}^{\text{inter}}(q,\omega) = \frac{i\hbar g}{4\pi^2} \int d\mathbf{k} \sum_n \sum_{m\neq n} \frac{\Delta f_{nm}}{\Delta E_{mn}} \frac{M_{mn}^{ij}}{\hbar\omega + i0^+ - \Delta E_{mn}} \tag{3.15}$$

$$\sum_n \sum_{m\neq n} A_{nm} = \sum_n \sum_{m\neq n} A_{mn} = 1/2 \sum_n \sum_{m\neq n} (A_{mn} + A_{nm})$$

$$= \frac{i\hbar g}{4\pi^2} \int d\mathbf{k} \sum_n \sum_{m\neq n} \frac{1}{2} \left\{ \frac{\Delta f_{nm}}{\Delta E_{mn}} \frac{M_{mn}^{ij}}{\hbar\omega + i0^+ - \Delta E_{mn}} + \frac{\Delta f_{mn}}{\Delta E_{nm}} \frac{M_{nm}^{ij}}{\hbar\omega + i0^+ - \Delta E_{nm}} \right\} \tag{3.16}$$

$$\Delta E_{mn} = -\Delta E_{nm}, \Delta f_{mn} = -\Delta f_{nm}$$

$$= \frac{i\hbar g}{8\pi^2} \int d\mathbf{k} \sum_n \sum_{m\neq n} \frac{\Delta f_{nm}}{\Delta E_{mn}} \left\{ \frac{M_{mn}^{ij}}{\hbar\omega + i0^+ - \Delta E_{mn}} + \frac{M_{nm}^{ij}}{\hbar\omega + i0^+ - \Delta E_{nm}} \right\} \tag{3.17}$$

$$M_{mn}^{ij} = M_{nm}^{ij*}$$

$$= \frac{i\hbar g}{8\pi^2} \int d\mathbf{k} \sum_n \sum_{m\neq n} \frac{\Delta f_{nm}}{\Delta E_{mn}} \left\{ \frac{M_{mn}^{ij}}{\hbar\omega + i0^+ - \Delta E_{mn}} + \frac{M_{mn}^{ij*}}{\hbar\omega + i0^+ + \Delta E_{mn}} \right\} \tag{3.18}$$

$$= \frac{i\hbar g}{8\pi^2} \int d\mathbf{k} \sum_n \sum_{m\neq n} \frac{\Delta f_{nm}}{\Delta E_{mn}}$$

$$\left\{ \frac{\hbar\omega \left(M_{mn}^{ij} + M_{mn}^{ij*} \right) + \Delta E_{mn} \left(M_{mn}^{ij} - M_{mn}^{ij*} \right)}{\hbar^2\omega^2 - \Delta E_{mn}^2} - i\pi \left[\delta(\hbar\omega - \Delta E_{mn}) M_{mn}^{ij} + \delta(\hbar\omega + \Delta E_{mn}) M_{mn}^{ij*} \right] \right\} \tag{3.19}$$

$$= \frac{i\hbar g}{8\pi^2} \int d\mathbf{k} \sum_n \sum_{m\neq n} \frac{\Delta f_{nm}}{\Delta E_{mn}} \left\{ \frac{\hbar\omega \left(M_{mn}^{ij} + M_{mn}^{ij*} \right) + \Delta E_{mn} \left(M_{mn}^{ij} - M_{mn}^{ij*} \right)}{\hbar^2\omega^2 - \Delta E_{mn}^2} - 2i\pi\delta(\hbar\omega - \Delta E_{mn}) M_{mn}^{ij} \right\} \tag{3.20}$$

$$\sigma_{ij}^{\text{inter}}(q,\omega) \simeq \frac{i\hbar g}{8\pi^2} \int d\mathbf{k} \sum_{n} \sum_{m\neq n} \frac{\Delta f_{nm} \left(M_{mn}^{ij} - M_{mn}^{ij*}\right)}{-\Delta E_{mn}^2} \tag{3.21}$$

$$= \frac{-i\hbar g}{4\pi^2} \int d\mathbf{k} \sum_{n} \sum_{m\neq n} \frac{\Delta f_{nm} \left(M_{mn}^{ij} - M_{mn}^{ij*}\right)}{2\Delta E_{mn}^2} \tag{3.22}$$

$$= \frac{-i\hbar g}{4\pi^2} \int d\mathbf{k} \sum_{n} \sum_{m\neq n} \left\{ \frac{f(E_n(\mathbf{k})) \left(M_{mn}^{ij} - M_{mn}^{ij*}\right)}{2\Delta E_{mn}^2} - \frac{f(E_m(\mathbf{k})) \left(M_{mn}^{ij} - M_{mn}^{ij*}\right)}{2\Delta E_{mn}^2} \right\} \tag{3.23}$$

$$= \frac{-i\hbar g}{4\pi^2} \int d\mathbf{k} \sum_{n} \sum_{m\neq n} \left\{ \frac{f(E_n(\mathbf{k})) \left(M_{mn}^{ij} - M_{mn}^{ij*}\right)}{\Delta E_{mn}^2} \right\} \tag{3.24}$$

$$= \frac{-i\hbar g}{4\pi^2} \int d\mathbf{k} \sum_{n} f(E_n(\mathbf{k})) \sum_{m\neq n} \frac{\left(M_{mn}^{ij} - M_{mn}^{ij*}\right)}{\Delta E_{mn}^2} \tag{3.25}$$

$$= \begin{cases} 0, & i = j \\ \\ \frac{-e^2 g}{4\pi^2 \hbar} \int d\mathbf{k} \sum_{n}, f(E_n(\mathbf{k}))\Omega_n^{ij}(\mathbf{k}), & i \neq j, \end{cases} \tag{3.26}$$

where $\Omega_n^{ij}(\mathbf{k}) = i \sum_{m\neq n} \frac{\langle n, \mathbf{k}| \frac{\partial H}{\partial k_i} |m, \mathbf{k}\rangle \langle m, \mathbf{k}| \frac{\partial H}{\partial k_j} |n, \mathbf{k}\rangle - h.c.}{\Delta E_{mn}^2} \tag{3.27}$

3.2.2 Two-Band Model

To better understand how this Berry Curvature effects the plasmon modes, we employ a Two-Band Model representing a gaped graphene system:

$$H = \hbar v(k_x \sigma_x + k_y \sigma_y) + m\sigma_z, \tag{3.28}$$

$$\hat{j}_x = ev\sigma_x \tag{3.29}$$

$$\hat{j}_y = ev\sigma_y \tag{3.30}$$

The eigenenergy and eigenstates of the wave vector $\mathbf{k}$ are:

$$E_\alpha(\mathbf{k}) = \alpha\sqrt{\hbar^2 v^2 k^2 + \Delta_g^2}, \tag{3.31}$$

$$|c, \mathbf{k}\rangle = \begin{pmatrix} \frac{e^{-i\phi}}{\sqrt{2}}\sqrt{1 + \frac{\Delta_g}{\sqrt{(\hbar\nu)^2 \mathbf{k}^2 + \Delta_g^2}}} \\ \frac{1}{\sqrt{2}}\sqrt{1 - \frac{\Delta_g}{\sqrt{(\hbar\nu)^2 \mathbf{k}^2 + \Delta_g^2}}} \end{pmatrix}, \tag{3.32}$$

$$|v, \mathbf{k}\rangle = \begin{pmatrix} \frac{e^{-i\phi}}{\sqrt{2}}\sqrt{1 - \frac{\Delta_g}{\sqrt{(\hbar\nu)^2 \mathbf{k}^2 + \Delta_g^2}}} \\ \frac{-1}{\sqrt{2}}\sqrt{1 + \frac{\Delta_g}{\sqrt{(\hbar\nu)^2 \mathbf{k}^2 + \Delta_g^2}}} \end{pmatrix} \tag{3.33}$$

$\alpha = c, v$ denote the conduction band and valence band, respectively and Δ_g is the band gap of the material. Applying the two band model we find the bulk plasmon frequency from the dielectric function in 2-dimensions:

$$\epsilon(q, \omega) = 1 + \frac{2\pi i q \sigma_{ii}(q, \omega)}{\omega} \tag{3.34}$$

Giving:

$$\omega^{bulk} = \frac{e}{\hbar}\sqrt{\frac{gq\beta}{2}} \tag{3.35}$$

$$\beta = \int_{\Delta_g}^{\infty} \frac{E_n^2 + \Delta_g^2}{E_n^2(f_c(\mathbf{k}))} + \int_{-\infty}^{-\Delta_g} \frac{E_n^2 + \Delta_g^2}{E_n^2(f_v(\mathbf{k}))} \tag{3.36}$$

The edge modes are the same as those found by Song 2016.(13)

$$\omega_{\pm}^{edge} = \sqrt{\frac{2}{3}}\omega_q^{bulk} \pm \frac{\sqrt{2}}{9}\mid q \mid \mathscr{F} + \mathscr{O}(q^2\mathscr{F}^2) \tag{3.37}$$
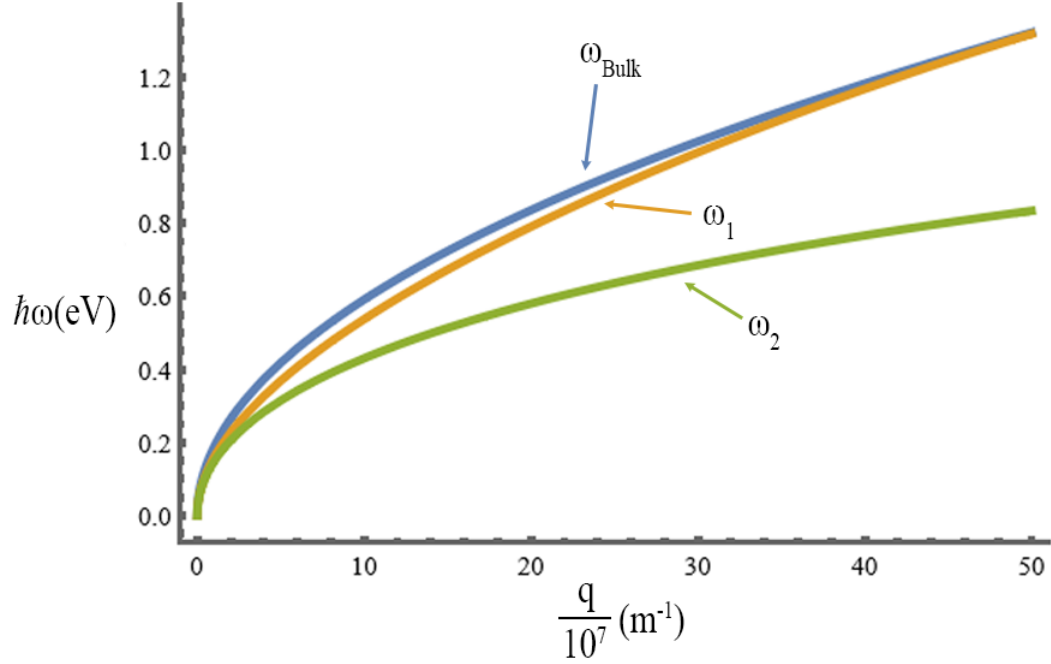
Figure 3.1 Here, $\omega_+^{edge} = \omega_1$ and $\omega_-^{edge} = \omega_2$. We can observe ω^{bulk} and ω_+^{edge} becoming indistinguishable as q increases. The next figures are results from our analysis of different values of Temperature(T), Fermi Level(μ), and Band Gap(Δ_g) of the material to find the largest values of $\omega^{bulk} - \omega_+^{edge}$. over the largest range of q values.

$\mathscr{F}$ is the Berry flux given by the solution for the interband solution of the Kubo formula in Eqn(9)

$$\mathscr{F} = \frac{-e^2 g}{4\pi^2 \hbar} \left(\int_{\Delta_g}^{\infty} dE \frac{\Delta_g}{E^2(f_c(\mathbf{k}))} + \int_{-\infty}^{-\Delta_g} dE \frac{\Delta_g}{E^2(f_v(\mathbf{k}))} \right) \tag{3.38}$$

3.3 Results

It is from these frequencies that we test under different theoretical states of quasi-equilibrium to determine which conditions allow for the largest separation of ω^{bulk} and ω_+^{edge}.
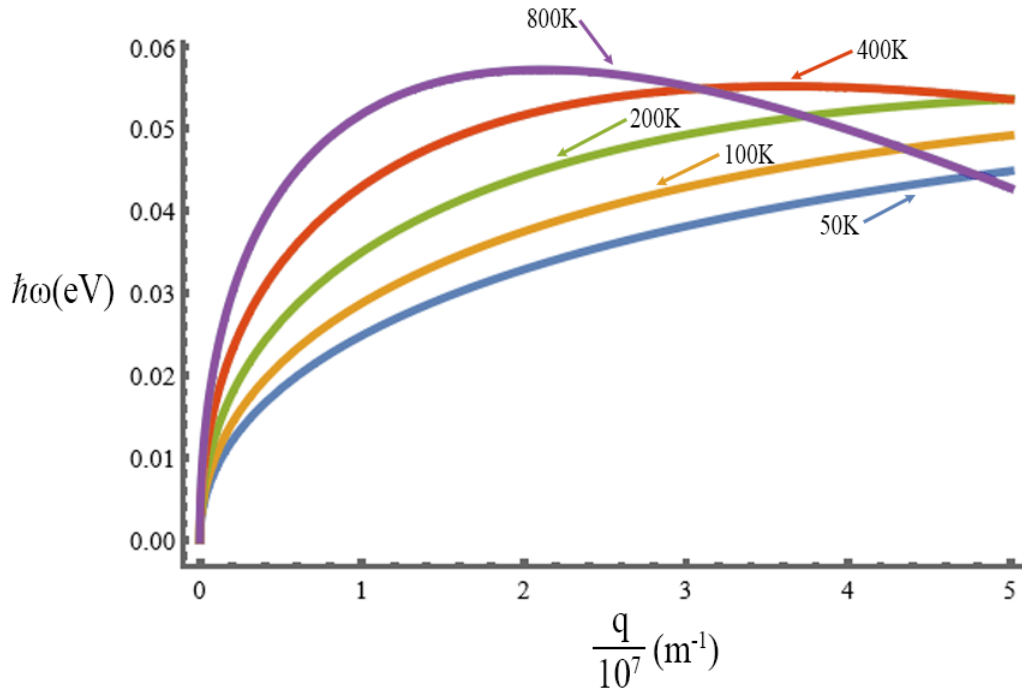
Figure 3.2 shows $\omega^{bulk} - \omega_+^{edge}$ for five different temperatures where the system is held in quasi-equilibrium. Showing for low values of q higher temperatures lead to higher separations of the bulk mode from the first edge mode. With $\mu = .1eV$ and $\Delta_g = 1eV$.

over the largest range of q values. Figure 1 shows the plasmon dispersion for the bulk and the edge modes.

In Figure 3.1, we have plotted the plasmon dispersion for $T = 100K$, $\mu = .1eV$, and $\Delta_g = 1eV$. This plot shows a plasmons dispersion that aligns with Ref(13) and Ref(9). Which shows for increasing values of q, only one mode continues to exist. The next theoretical trials we ran hold two of the external variables constant in equations 19 and 21 and varies only one. Either temperature(T), Fermi Level(μ), or band gap(Δ_g).

In Figure 3.2, we assumed the system was stimulated to a higher temperature, but decayed to a certain value where the system was held in a state of quasi-equilibrium. This could be represent the
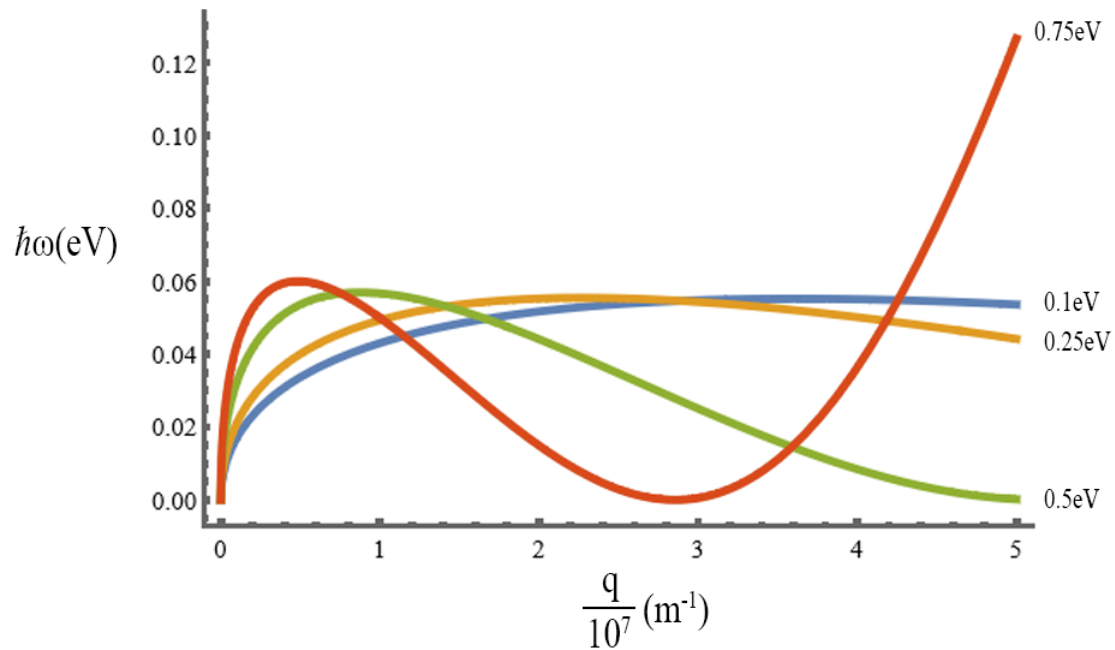
Figure 3.3 is a similar plot but with different quasi-Fermi levels. This shows that for large Fermi levels, large separations do exist at small q, however they quickly join the bulk frequency unlike smaller Fermi levels which maintain a larger separation for a larger range of q values.

material "heating up" during optical pumping to achieve valley polarization and not returning to a low Kelvin value. Figure 2 shows that while higher temperatures creating larger initial separations of ω^{bulk} and ω_+^{edge}, they also lead to the modes combining at lower q values. Therefore, lower temperatures produced a wider range of q values for two chiral modes to exist.

Figure 3.3 shows the next case where temperature and band gap where held constant while the Fermi level at which the valleys in the gaped graphene system were populated to varied. This case is achieved by applying different strengths of circularly polarized light at the system, resulting in different levels of valley polarization. Higher applied field amplitudes correspond with higher levels of valley polarization.(29). We also see that, unsurprisingly, the Fermi level acts similarly to
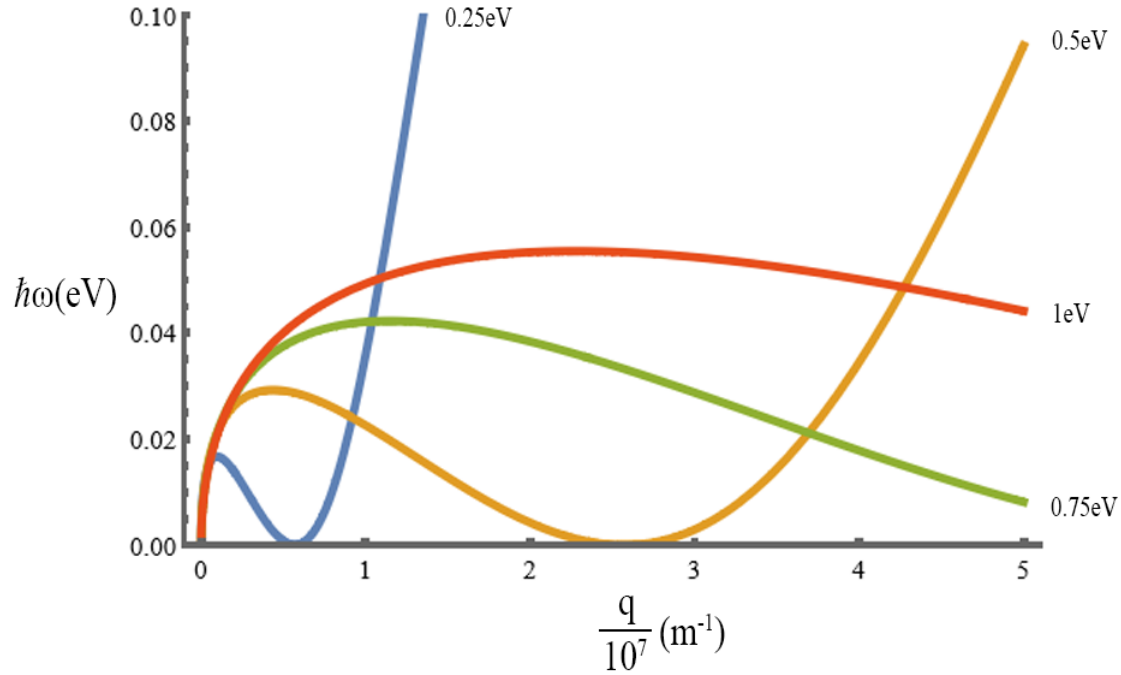
Figure 3.4 shows four different values of Band Gap in the material. Opposite of larger Fermi values, larger values of Band Gap lead to larger separations for a larger range of q values.

varying the temperature in Figure 2. As higher Fermi levels create short-lived large separations of ω^{bulk} and ω_+^{edge}. The value of $\omega^{bulk} - \omega_+^{edge}$ diverges after reaching zero as well. This phenomena is due to the modes becoming indistinguishable. A key feature of our system aligns with how valley polarization acts as shown in Ref(29). Valley polarization decreases with larger incoming field amplitudes meaning that higher Fermi levels would also have lower levels of valley polarization. Therefore the Berry flux would eventually fall to zero and both modes would cease to exist.

Finally, Figure 3.4 shows the final theoretical case where the varying variable was the system's band gap. We continued to simulate this with a gaped graphene system, however this could be achieved by using different materials like different transition metal dichalcogenides (TMDCs) with varying natural band gaps. It is here we find the opposite of the other cases where larger band

gaps are preferred for a wider range of q values with two chiral Berry plasmon edge modes. Larger band gaps also lead to larger separations of ω^{bulk} and ω_+^{edge} even though it still peaks at $60meV$.

3.4 Conclusion

In this chapter we have shown multiple ways to vary the Berry flux of a gaped graphene system to alter the chiral Berry plasmon edge modes that arise without magnetic field. These methods would vary the splitting between the two edge modes analogously to altering the magnetic field in magnetoplasmons. More importantly though, we have shown a possible way to ensure that both chiral edge modes exist for a larger range of values by ensuring the system has a large band gap, low equilibrium temperature and low level of valley polarization.

CHAPTER 4
SPASERS

4.1 Introduction

For nearly two decades now, SPASER (Surface Plasmon Amplification by Stimulated Emission of Radiation) research has bloomed into a well-defined field in physics. Spaser research originated in 2003 and has similar goals of pushing forward infrared spectroscopy, sensing, probing, and biomedical treatment as the laser before it.(30) SPASERs are a continuation of lasers in that they achieve miniaturization below the half wavelength limit of a laser. This implies that a spasing system is much better suited to probing biological systems below 10nm and for use in technological marvels such as 10nm transistors.(7) The SPASER is our best attempt at gaining a coherent, intense, ultrafast (with pulse duration down to a few femtoseconds), source of optical energy concentrated down to the nanoscale.(31) The use of plasmonic nanoparticles to concentrate optical energy due to plasmonic resonance and geometric concentration in nanoscopy, nanospectroscopy, and nanoscale detection is also experimentally proven.(32)(33)(12)(34)

The SPASER and LASER share a similar theoretical philosophy. Both systems require an externally pumped active medium and take advantage of stimulated emission. However, instead of a resonant cavity like in a LASER, a SPASER uses a single nanoparticle that supports plasmonic modes. This leads to the vital difference between the two: A SPASER "ideally" operates without any photons. Surface plasmons replace photons entirely in the working operation of the SPASER, and theoretically, an ideal nanoscale source would also generate. 'dark' optical modes that do not couple to far-field zones.(31)

Even though SPASERs are similar to LASERs, the need for SPASERs to exist arises from their

ability to deliver a source of intense optical energy and much smaller scales than the LASER. A LASER is limited in size because photons can only exist above the diffraction limit, but surface plasmons are not subjected to this limit. This is because nano-optical fields are purely electric oscillations at optical frequencies. When electromagnetic waves are contained at sizes much smaller than a wavelength, the magnetic field component does not significantly contribute. At this scale, optical modes are localized on smaller dimensions than the optical wavelength. These modes are what we classify as surface plasmons. Essentially, surface plasmons are the eigenmodes of a material system that correspond to oscillations of the electron liquid at optical frequencies.

Surface plasmons also act mathematically similarly to photons. First, surface plasmons are bosons: they are vector excitations and have spin 1, similar to photons. Second, surface plasmons are electrically neutral excitations. Furthermore, third, surface plasmons are the most collective material oscillations known in nature, which implies they are the most harmonic, meaning they interact very weakly with one another. As such, surface plasmons can undergo stimulated emission, accumulating in a single mode in large numbers, which is the physical foundation of both the LASER and the SPASER.(31)

As mentioned in Chapter 2, a system must contain both positive and negative permittivity for surface plasmons to exist. Even though negative permittivity materials do not allow electromagnetic waves to propagate entirely, they do exist for at least a skin depth length within the material. This skin depth length is the characteristic scale for a SPASER. The nanoparticles acting as the SPASER's resonant cavity are smaller than most metals' skin depth lengths. This allows electromagnetic waves to penetrate their entire volume before the wave decays and drives surface plasmon oscillations.
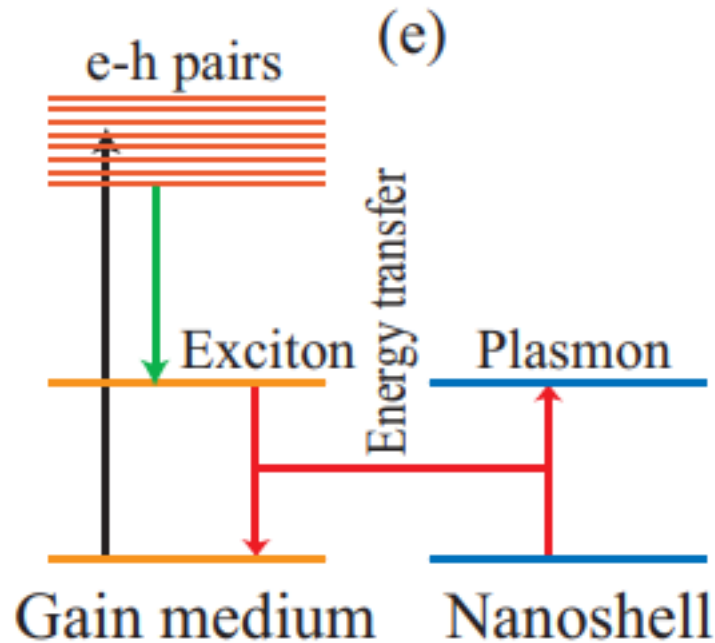
Figure 4.1 is from Ref(5) and shows a simple diagram of the working mechanism of the SPASER.

4.2 Qualitative Explanation of a SPASER

Once the nanoparticle is properly within the skin depth length of the metal and an electromagnetic wave has penetrated its entire volume, the electric oscillations between the gain medium and the generation of plasmons along the nanoparticle surface begin to couple.(35)

This is shown in Fig 4.1. The external field stimulates excitons from the ground state in the gain medium to an excited state. When these decay back to the ground state, the energy is transferred to the nanoparticle, creating a surface plasmon. A fundamental process within this transition is that the plasmonic oscillations generate an electric field that re-stimulates the gain medium. This feedback mechanism inherent to the SPASER is responsible for causing the stimulated emission

process necessary for the laser-like functioning of the SPASER. The feedback mechanism of the SPASER cannot be removed as well. This leads to the SPASER always developing generation and accumulating the macroscopic number of coherent surface plasmons in the spasing mode.(5)

4.3 Theoretical Methods

The first step of deriving a SPASER theoretically is by determining the eigenmodes described in the previous section:

$$\nabla\theta(\mathbf{r})\nabla\psi_n(\mathbf{r}) = s_n\nabla^2\psi_n(\mathbf{r}) \tag{4.1}$$

s_n is the eigenvalue of the nth modes contained within the range $1 \geq s_n \geq 0$, while θ is simply a characteristic function equal to 1 inside and 0 outside the metal. The eigenmodes are normalized by an integral over the volume V of the system:

$$\int_V |\nabla\phi_n(\mathbf{r})|^2 d^3\mathbf{r} = 1 \tag{4.2}$$

Determining the dynamics of a SPASER requires using the Quantum Density Matrix or the Optical Bloch Equations. This is a similar procedure for determining the theoretical dynamics of a LASER and is also applicable here because of the similarities between LASERs and SPASERs. Most research treats this system semi-classically, where the active medium is viewed entirely through quantum mechanics; however, the surface plasmons are considered classical quantities.

The Hamiltonian of the Spasing system is:

$$H = H_{sp} + H_{gain} + H_{int} \tag{4.3}$$

H_{sp} is the Hamiltonian of the surface plasmons themselves:

$$H_{sp} = \hbar\omega_{sp} \sum_n \hat{a}_n^* \hat{a}_n \tag{4.4}$$

$\hat{a}_m^*$ and $\hat{a}_m$ are the creation and annihilation operators. This is where the surface plasmons (SPs), including the creation and annihilation operators, can be treated as quasi-classical quantities $a_n = a_{0n}e^{-i\omega t}$ With a_{0n} as a slowly varying amplitude. This allows us to classify the number of plasmons per mode at a given time as $N_p = |a_{0n}|^2$. H_{gain} is the Hamiltonian of the gain medium in the system and H_{int} is the Hamiltonian of the electric field operator's interaction with the plasmons' dipole moment operator.

$$H_{int} = \int \sum_n \mathbf{E}_n(\mathbf{r})\hat{\mathbf{d}}_n(\mathbf{r})d^2\mathbf{r} \tag{4.5}$$

$$E_n = -\sum_n A_n \nabla\psi_n(\mathbf{r})(\hat{a}_n + \hat{a}_n) \tag{4.6}$$

$$A_n = (\frac{4\pi\hbar s_n}{\epsilon_d s_n'})^{\frac{1}{2}} \tag{4.7}$$

These are the most general equations for SPASER systems. In 2009, Dr. Stockman derived this method for a two-level gain medium.(5) Realistically, the gain medium would have three or four states active during optical transitions. The two-level approximation works because the relaxation rate between the highest and highest levels is incredibly fast, as is the relaxation rate between

the bottom working and bottommost levels of the system. Because of this, we can consider these rates nearly infinite, as if the system only pumps electrons from the lower working level to the top. However, in 2018 Dr. Stockman and Dr. Apalkov instructed Dr. Ghimire and me to consider these transitions in deriving a more in-depth theoretical analysis of the density matrix approach to the SPASER, and that is where this Chapter will focus.

4.4 Three Level SPASER

The three-level SPASER's gain medium contains three quantum levels: $|0\rangle, |1\rangle$, and $|2\rangle$. The system is pumped by external radiation, which causes electrons to jump from $|0\rangle$ to $|2\rangle$ with the transition (gain) rate g. The excited states of the system are also characterized by relaxation rates γ_{21} and γ_{10}, which represent the transitions $|2\rangle \rightarrow |1\rangle$ and $|1\rangle \rightarrow |0\rangle$ respectively. The gain medium is coupled to the plasmonic system through the field-dipole interaction, and it is at the almost resonant condition with the frequency ω_{12} is close to the surface plasmon frequency, ω_{sp}.

This project aimed to have theoretical calculations more closely represent the experimental results found in Ref(8). Because of this, we needed to change the SPASER Laplace equation better to represent the presence of three mediums in the system to calculate the field of the Localized Surface Plasmons. In the spherical system, we consider the electric potential of the dipole mode to be of the form:

$$\phi_i(\mathbf{r}) = (\frac{a_i}{r^2} + b_i r) Y_{10}(\mathbf{r}) \tag{4.8}$$

where i labels the medium ($i = 1, 2, 3$), a_i and b_i are coefficients corresponding to medium i, and $Y_{10}(\mathbf{r})$ is a spherical harmonics ($l = 1$ and $m = 0$). The following expressions give Maxwell's

continuity equations across the interfaces of the layers:

$$\phi_i(\mathbf{r}_i) = \phi_{i+1}(\mathbf{r}_i) \tag{4.9}$$

$$\epsilon_i \frac{\partial}{\partial r} \phi_i(\mathbf{r}_i) = \epsilon_{i+1} \frac{\partial}{\partial r} \phi_{i+1}(\mathbf{r}_i) \tag{4.10}$$

where ϵ_i is the permittivity of medium i. For our system, which consists of 3 layers, silver sphere, dye, and water, we solve Eqs. (4.9) and (4.10) to obtain permittivity of silver 3 ϵ_s as a function of the permittivity of dye ϵ_d and water ϵ_{H_2O}. The frequency of Localized Surface plasmons is then obtained by equating ϵ_s to the experimental value $\epsilon_{Ag}(\omega)$. (?)

$$\epsilon_s(\epsilon_d, \epsilon_{H_2O}) = Re[\epsilon_{Ag}(\omega_{sp})] \tag{4.11}$$

The specific SPASER Hamiltonian to this configuration is similar to equations 4.5, 4.6, and 4.7. However, the electric field operator is:

$$E_n = -\sum_n A_{sp} \nabla \psi_n(\mathbf{r})(\hat{a}_n + \hat{a}_n) \tag{4.12}$$

$$A_{sp} = \left(\frac{4\pi\hbar}{\frac{d}{d\epsilon_{Ag}} s_1}\right)^{\frac{1}{2}} \tag{4.13}$$

Here, the geometrical parameter s_1 is given by the following expression:

$$s_1 = \frac{\int_{V_{metal}} |\nabla\phi_i(\mathbf{r})|^2 d^3\mathbf{r}}{\int_{-\infty}^{\infty} |\nabla\phi_i(\mathbf{r})|^2 d^3\mathbf{r}} \tag{4.14}$$

4.4.1 SPASER Dynamics

Deriving the dynamical SPASER equations for the three-level system is similar to the two-level system, just surprisingly, with one additional quantum state. First, we begin with the Heisenberg representation of quantum mechanics, where the quantum operators vary in time, and the state vectors are time-independent. This method is also easy to grasp because you can think of the electric field and dipole moments varying while the energy levels within the gain are always constant. The Heisenberg Equation of Motion is:

$$i\hbar\dot{\hat{\rho}}(\mathbf{r}, \mathbf{t}) = [\hat{\rho}(\mathbf{r}, \mathbf{t}), \hat{H}] \tag{4.15}$$

We can see from this equation that the time dependence of an operator is determined by its commutator with the specific Hamiltonian of the system, $H = H_{sp} + H_{gain} + H_{int}$. Therefore, to determine all the necessary relations for the dynamical spasing equations, we need to find and solve the Heisenberg Equation of Motion for all necessary operators: $\hat{\rho}$, $\hat{n}$, and $\hat{a}$.

$$i\hbar\dot{\hat{\rho}}(\mathbf{r}, \mathbf{t}) = [\hat{\rho}(\mathbf{r}, \mathbf{t}), \hat{H}] \tag{4.16}$$

$$i\hbar\dot{\hat{n}}(\mathbf{r}, \mathbf{t}) = [\hat{n}(\mathbf{r}, \mathbf{t}), \hat{H}] \tag{4.17}$$

$$i\hbar\dot{\hat{a}}(\mathbf{r}, \mathbf{t}) = [\hat{a}(\mathbf{r}, \mathbf{t}), \hat{H}] \tag{4.18}$$

The operator $\hat{\rho}$ describes the transition between energy levels within the gain medium, and we must solve equation 4.16 for each likely transition between the three levels. $\hat{n}$ is the operator that,

when applied to the quantum states, gives us the population of that state as an eigenvalue. $\hat{a}$ is the creation and annihilation operator, which we can use later to determine the number of plasmons in the system.

Before we continue, we will also apply the Rotating Wave Approximation. This way we can ignore the rapidly oscillating terms and only focus on the necessary terms.

It is a simple procedure, and it gives us our necessary equations:

$$\dot{\rho}_{10}(\mathbf{r}) = [i(\omega - \omega_{10} - \Gamma_{10}]\rho_{10}(\mathbf{r}) + in_1\Omega_{10}^*(\mathbf{r})a_0^* \tag{4.19}$$

$$\dot{n}_2 = gn_0 - \gamma_{21}n_2 \tag{4.20}$$

$$\dot{n}_1 = -\gamma_{10}n_1 + \gamma_{21}n_2 - 2\int_V Im[\rho_{10}(\mathbf{r})\Omega_{10(\mathbf{r})}a_0] \tag{4.21}$$

$$\dot{n}_0 = -gn_0 + \gamma_{10}n_1 + 2\int_V Im[\rho_{10}(\mathbf{r})\Omega_{10(\mathbf{r})}a_0] \tag{4.22}$$

where ω_{10} is the transition frequency between $|1>$ and $|0>$ levels of the gain medium, and g is the excitation rate from the $|0>$ level to the $|2>$ level by an external pulse. In the above equations, we also introduced the relaxation rates: polarization relaxation rate Γ_{10} and the spontaneous relaxation rates γ_{10} and γ_{21} between the corresponding states as indicated by the indices.

Using the creation and annihilation operators, we derive the system's equation of motion for surface plasmons.

$$\dot{a} = a_0\gamma_{sp}(\omega) + i(\omega - \omega_{sp})a_0 + i\int_V (\rho_{10}^*(\mathbf{r})\Omega_{10}^*(\mathbf{r}))d^3\mathbf{r} \tag{4.23}$$

γ_{sp} is the plasmon relaxation rate:

$$\gamma_{sp} = \frac{Im[\epsilon_{Ag}(\omega)]}{Re[\frac{\partial \epsilon_{Ag}(\omega)}{\partial \omega}]} \tag{4.24}$$

This relaxation rate is tied to the transition between levels $|1>$ and $|0>$ because the surface plasmons are generated by the decay of exictons in the gain medium. This can also be seen in the expression for γ_{10}:

$$\gamma_{10} = |\Omega_{10}|^2 \frac{2(\gamma_{sp} + \Gamma_{10})}{(\omega_{sp} - \omega_{10})^2 + (\gamma_{sp} + \Gamma_{10})^2} \tag{4.25}$$

These are all the necessary equations for determining the dynamics of the three-level SPASER.

4.4.2 Continuous Wave Regime

Analytically we can derive the spasing equations for the continuous wave regime where the time derivatives of the operators are equal to zero. We can introduce a simple term for the population inversions within the system as well:

$$n_{10} = n_1 - n_0 \tag{4.26}$$

$$n_{21} = n_2 - n_1 \tag{4.27}$$

The populations are also normalized so that $n_0 + n_1 + n_2 = 1$, so we can use these relations to express the stationary terms for the populations in terms of the working transition n_{10}.

$$n_0 = \frac{\gamma_{21} n_{10} - \gamma_{21}}{2\gamma_{21} + g} \tag{4.28}$$

$$n_1 = -\frac{-\gamma_{21} - g n_{10} - \gamma_{21} n_{10}}{2\gamma_{21} + g} \tag{4.29}$$

$$n_2 = -\frac{g n_{10} - g}{2\gamma_{21} + g} \tag{4.30}$$

Substituting these new relations into the static versions of equations 4.19-4.23 we obtain:

$$\rho_{10}(\mathbf{r}) = -\frac{a_0^* n_{10} \Omega_{10}^*(\mathbf{r})}{i\Gamma_{10} - \omega_s + \omega_{10}} \tag{4.31}$$

$$n_{10} = \frac{(\omega_s - \omega_{sp})(\omega_{10} - \omega_s) + \gamma_{sp}\Gamma_{10}}{V \rho_{10} \Omega_{10}^2} \tag{4.32}$$

$$N_n = |a_0|^2 = \frac{\Gamma_{10}^2 + (\omega_s - \omega_{10})^2}{2n_{10}\Gamma_{10}} \tag{4.33}$$

$$\times \frac{\gamma_{21}(g - \gamma_{10} - n_{10}(\gamma_{10} + g)) - \gamma_{10} g n_{10}}{(2\gamma_{21} + g)\Omega_{10}^2}$$

Equations 4.25 and 4.33 will also let us derive an expression for the spasing frequency:

$$\omega_s = \frac{\omega_{10}\gamma_{sp} + \Gamma_{10}\omega_{sp}}{\Gamma_{10} + \gamma_{sp}} \tag{4.34}$$

The key take away from the above expressions is that they are analytic expressions for the effect of γ_{21} on the spasing equations. γ_{21} was ignored in Ref(5) and separates this chapter from that work. We can see from equations 4.31 to 4.34 that the relaxation rate from the third level to the second has no effect on population inversion or the spasing frequency but it does have an effect in equation 4.33, the number of plasmons generated.

If we take γ_{21} to approach $\frac{1}{\infty}$, then equation 4.33 becomes identical to the two-level system.

$$N_n = |a_0|^2 = \frac{\Gamma_{10}^2 + (\omega_s - \omega_{10})^2}{2n_{10}\Gamma_{10}}$$
$$\times \frac{-\gamma_{10}n_{10}}{\Omega_{10}^2}$$

(4.35)

CHAPTER 5

ULTRA-FAST PULSE PUMPING OF A TOPOLOGICAL SPASER

5.1 Introduction

A recent focus has been on a new sub-field of spasers, topological spasers.(36)(37)(38) Here, we thoroughly examine a type II topological spaser. Only the gain medium has topological properties, and the plasmonic material is a silver nanospheroid. We build upon the foundation of previous works by investigating the screening effects of the silver spheroid on the incoming optical pumping and the nonuniform excitation of the transition metal dichalcogenide (TMDC) layer. Our system's topological gain medium is a circular TMDC monolayer flake. TMDC layers contain band gaps at its K and K' points in reciprocal space.(29) The valleys from these band-gaps are degenerate, protected by time reversal symmetry, and have chiral electron states with opposite topological charges. Previous work has shown that populations in the TMDC's K and K' valleys can be selected explicitly by circularly polarized optical pumping in a process called valley polarization.(29)

A type II topological spaser has two spasing modes denoted by the azimuthal quantum numbers,
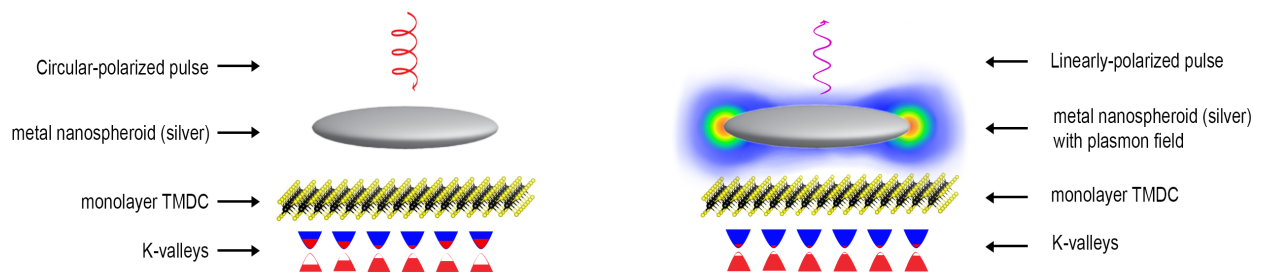
Figure 5.1 Figure 4.1.A shows a circularly polarized pulse incident onto a metal nanospheroid and TMDC monolayer. Below is a diagram of the K-Valleys in the TMDC, with the outermost valleys being populated more than the innermost valleys. Figure 4.1.B shows the system a few picoseconds later as surface plasmons are generated along the metal nanospheroid, and the system emits linearly-polarized radiation.
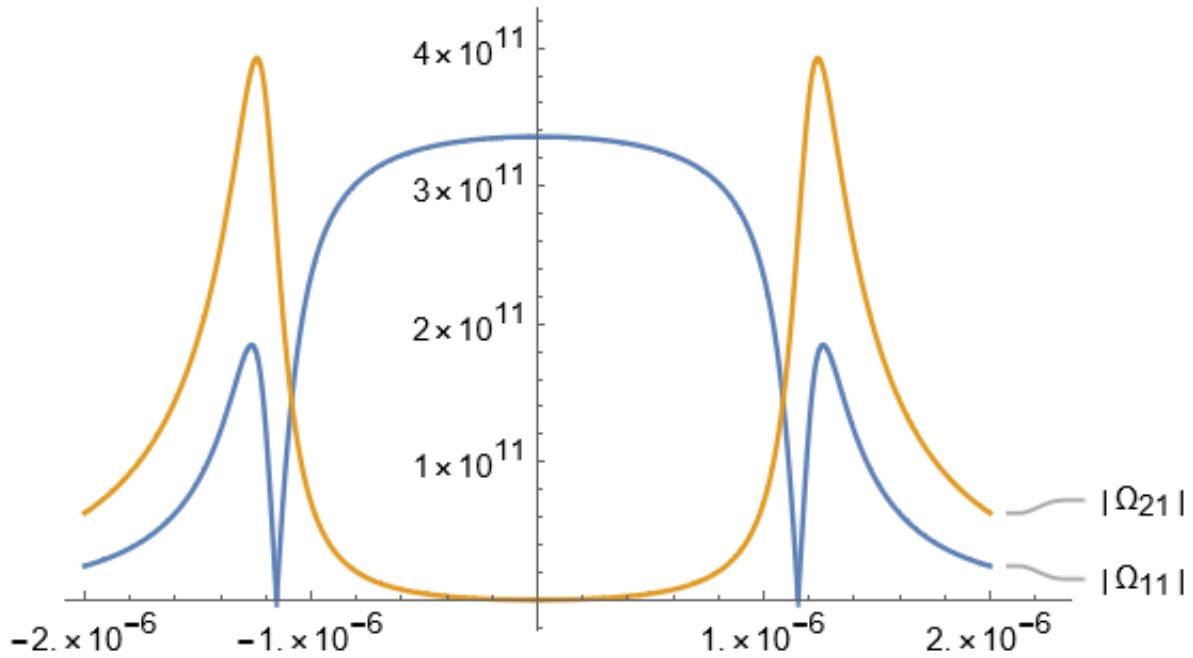
Figure 5.2 The Rabi Frequency of both plasmons modes

$m = 1$ and $m = 1$. When the TMDC flake radius is small relative to the spheroid, each mode is strongly coupled to one of the TMDC valleys, K for $m = 1$ and K' for $m = 1$, therefore applying either a right or left handed circularly polarized pulse to the TMDC should determine the resultant spasing mode. These modes are topologically protected, as shown in Ref(36). Another interesting phenomenon associated with type II spasers is the dependence of the mode on the size of the TMDC flake.(37) If the TMDC flake has a larger radius than the primary axis of the nanosphere, then we should see two spasing regimes. One where the spaser acts as described above and another where both spasing modes exist. This should allow us to generate either one singular plasmon mode, only $m = 1$ or $m = 1$, or two plasmon modes, $m = 1$ and $m = 1$. This is due to the modes coupling to the Rabi frequency of the spasing transition and the behavior of the Rabi frequency.

A plot of the Rabi frequency is given in Fig 5.2.

To describe its behavior, two regimes within it are responsible for the TMDC radius dependence of the modes. Directly underneath the nanospheroid, the Rabi frequency is significant for $\Omega_{1,K}$ and $\Omega_{1,K'}$ and nearly zero for the opposite couplings. Along the edges of the nanospheroid, the Rabi frequency shows a strong coupling to both modes because of the dipole nature of the plasmonic field in the area close, but not in, the nanospheroid. We discovered during our initial simulations that the silver nanospheroid screened the area underneath it from the incoming pulse to pump it. This forced us to choose a radius of TMDC larger than the spheroid so that the peaks in the field around the edges could potentially correctly populate the TMDC valleys. The spasing system also experiences loss in the form of emitted radiation.

Far-field radiation is not the goal of the spaser, but recent work has also shown its promise in creating nanolasers.(37) Nanolasers have potential applications in biomedical research for the diagnosis and therapeutics of cancer.(8) In our specific system, though, we see the spaser as creating a solid source of amplification of the incoming pulse. In addition, far-field radiation also shifts polarization after contributing to the spasing system. This is more supporting evidence that the topological spaser has potential as an excellent far-field radiation source and is explored in detail as the last step of this research.

5.2 Theoretical Methods

Our methods can be summarized qualitatively as simulating a fast pulse impacting the system, determining the electric field due to the silver nanospheroid in the presence of the external field, calculating the resultant conduction band populations in the TMDC monolayer, and finally using those populations as a basis for population inversion required in the spasing system.

5.2.1 Equations of the Incident Pulse

The external field in our case is an incoming pulse characterized as a strong circularly-polarized optical field with a duration of a few fs and amplitude $F < 1V\mathring{A}^{-1}$. As shown in Figure 4.1, the TMDC monolayer lies in the x-y plane along with the nanospheroid. The incident pulse approaches the system parallel along the x axis. We assumed the pulse could be approximated by a uniform field initially as after the pulse ends the resultant electric is due to the eigenmodes of the surface plasmons along the spheroid. Where the elliptical coordinates used were:

$$x = a\sqrt{1+\zeta^2}\sqrt{1-\eta^2}\cos\phi \tag{5.1}$$

$$y = a\sqrt{1+\zeta^2}\sqrt{1-\eta^2}\sin\phi \tag{5.2}$$

$$z = a\zeta\eta \tag{5.3}$$

The limits being: $0 \leq \zeta < \infty, -1 \leq \eta \leq 1$, and $0 \leq \phi \leq 2\pi$

We went about this in the usual way with separation of variables. With the Laplacian in our coordinate system being:

$$\nabla^2\Phi = \frac{1}{a(\zeta^2-\eta^2)}[\sqrt{\zeta^2-1}\frac{\partial\Phi}{\partial\zeta}(\sqrt{\zeta^2-1}\frac{\partial\Phi}{\partial\eta}) \tag{5.4}$$
$$+\sqrt{1-\eta^2}\frac{\partial\Phi}{\partial\eta}(\sqrt{1-\eta^2}\frac{\partial\Phi}{\partial\eta})$$
$$+\zeta\frac{\partial\Phi}{\partial\zeta}-\eta\frac{\partial\Phi}{\partial\eta}]+\frac{1}{a^2(\zeta^2-1)(1-\eta^2)}\frac{\partial^2\Phi}{\partial\phi^2}$$

Following Ref(39) for an ellipsoid in a uniform electric field, we have a potential with two parts:

$$\Phi = \Phi_0 + \Phi_1 \tag{5.5}$$

Φ_0 is representative of the uniform field and Φ_1 contains the specific contribution of the spheroid.

$$\Phi_0 = -E_o Z(\zeta) H(\eta) \cos \phi \tag{5.6}$$

$$\Phi_1 = \begin{cases} \Phi_0 + C_1 a Z_1(\zeta) H(\eta) \cos \phi, & \zeta < \zeta_0 \\ \\ \Phi_0 + C_2 a Z_2(\zeta) H(\eta) \cos \phi, & \zeta > \zeta_0 \end{cases} \tag{5.7}$$

$Z_1(\zeta)$ is simply $\sqrt{\zeta^2 - 1}$ and $Z_2(\zeta)$ is $\sqrt{\zeta^2 - 1}(\frac{2\zeta}{\zeta^2-1}+\ln \frac{\zeta-1}{\zeta+1})$. C_1 and C_2 are the constants we need to solve for using the appropriate boundary conditions: $\Phi_{in} = \Phi_{out}$, when $\zeta = \zeta_0$ and $\epsilon_1 \frac{\partial \Phi_{in}}{\partial \zeta} = \epsilon_2 \frac{\partial \Phi_{out}}{\partial \zeta}$ on the surface of the spheroid.

$$C_1 = C_2 \frac{Z_2(\zeta_0)}{Z_1(\zeta_0)} \tag{5.8}$$

$$C_2 = \frac{(\epsilon_2 - \epsilon_1) E_0 \frac{dZ_1(\zeta_0)}{d\zeta} Z_1(\zeta_0)}{\epsilon_2 \frac{dZ_2(\zeta_0)}{d\zeta} Z_1(\zeta_0) - \epsilon_1 \frac{dZ_1(\zeta_0)}{d\zeta} Z_2(\zeta_0)} \tag{5.9}$$

This is the solution for the initial pulse incident onto the spheroid. The electric field due to the eigenmodes of the surface plasmons is found using Ref(30).

$$\nabla[\theta(\mathbf{r}) \nabla \phi_m] = s_{sp} \nabla^2 \phi_m \tag{5.10}$$

$\theta(\mathbf{r})$ is the characteristic function equal to 1 in the spheroid and 0 everywhere else. $l = 1$ is multipole

quantum number and m is the angular momentum projection. The solution for the eigenmodes is:

$$\phi_m = C_N P_1^m(\eta) e^{im\phi} \begin{cases} \frac{P_1^m(i\zeta)}{P_1^m(i\zeta_0)}, & \zeta < \zeta_0 \\[12pt] \frac{Q_1^m(i\zeta)}{Q_1^m(i\zeta_0)}, & \zeta_0 < \zeta \end{cases} \tag{5.11}$$

$P_l^m(x)$ and $Q_l^m(x)$ are the Legendre functions of the first and second kind. The constant C_N is determined by the normalization condition of the eigenmodes:

$$\int_{-\infty}^{\infty} |\nabla \phi_m(\mathbf{r})|^2 d^3\mathbf{r} = 1 \tag{5.12}$$

We follow methods previously defined by Motlagh for determining the conduction populations in TMDC. We use a three-band tight binding model Hamiltonian and describe the electron dynamics as coherent by the time-dependent Schrodinger equation (TDSE) with an interaction representation in an adiabatic basis of the Houston functions $\Psi_{\mathbf{q}}^{(H)}(\mathbf{r}, t)$. (29)

$$\Psi_{\mathbf{q}}(\mathbf{r}, t) = \sum_{\alpha=c_1,c_2,\nu} \beta_{\alpha\mathbf{q}}(t) \Phi_{\alpha\mathbf{q}}^{(H)}(\mathbf{r}, t) \tag{5.13}$$

Here, v, c_1, c_2 denote the highest valence band and the two lowest conduction bands, respectively while $\beta_{\alpha\mathbf{q}}(t)$ are the expansion coefficients satisfying the following equations:

$$\frac{d\beta_{\alpha\mathbf{q}}(t)}{dt} = \frac{-i}{\hbar} \sum_{\alpha_1 \neq \alpha} \mathbf{F}(t) \mathbf{Q}_{\alpha\alpha_1}(\mathbf{q}, t) \beta_{\alpha_1\mathbf{q}}(t) \tag{5.14}$$

where,

$$\mathbf{Q}_{\alpha\alpha_1}(\mathbf{q}, t) = \mathbf{D}_{\alpha\alpha_1}[(\mathbf{k}(\mathbf{q}, t)]e^{i\phi^{(d)}_{\alpha\alpha_1}(\mathbf{q},t)} \tag{5.15}$$

$$\phi^{(d)}_{\alpha\alpha_1}(\mathbf{q}, t) = \frac{-i}{\hbar} \int_{-\infty}^{t} \left(E_\alpha[(\mathbf{k}(\mathbf{q}, t')] - E_{\alpha 1}[(\mathbf{k}(\mathbf{q}, t')]\right) dt' \tag{5.16}$$

$$\mathbf{D}_{\alpha\alpha_1} = e\mathbf{A}_{\alpha\alpha_1} \tag{5.17}$$

$$\mathbf{A}_{\alpha\alpha_1}(\mathbf{q}) = \langle \Psi_\mathbf{q}^\alpha | \, i\frac{\partial}{\partial \mathbf{q}} \, |\Psi_\mathbf{q}^{\alpha_1}\rangle \tag{5.18}$$

The total population of the conduction bands are defined as $N_c(\mathbf{q}, t) = |\beta_{c_1\mathbf{q}}(t)|^2 + |\beta_{c_2\mathbf{q}}(t)|^2$. $N_c(\mathbf{q}, t)$ can be then interpreted as the total population inversion to be used in the spasing system of the nanosphere. Equations 1 through 6 employ a Three-Band Model; however, when applying these equations to the spasing system, we approximate the result with a Two-Band Model. The Two-Band non-Abelian Berry connection in reciprocal space and the transition dipole element is:

$$\mathbf{D}_{cv} = e\mathbf{A}_{cv} \tag{5.19}$$

$$\mathbf{A}_{cv}(\mathbf{k}) = \langle \Psi_\mathbf{k}^c | \, i\frac{\partial}{\partial \mathbf{k}} \, |\Psi_\mathbf{k}^v\rangle \tag{5.20}$$

In the Two-Band Model for the spaser, the approximated population is:

$$N_c(\mathbf{q}, t) = |\beta_{c\mathbf{q}}(t)|^2 \tag{5.21}$$

5.2.2 Equations of the Spasing System

As first derived by Bergman and Stockman 2003, the plasmonic eigenmodes of a nanospheroid are described quasi-statically as:

$$\nabla\theta(\mathbf{r})\nabla\psi_n(\mathbf{r}) = s_n\nabla^2\psi_n(\mathbf{r}) \tag{5.22}$$

s_n is the eigenvalue of the nth modes contained within the range $1 \geq s_n \geq 0$, while θ is simply a characteristic function equal to 1 inside and 0 outside the metal. Our oblate nanospheroid inherently has azimuthal symmetry. Therefore, the eigenmodes are described by two spheroidal quantum numbers: multipolarity l and azimuthal quantum number m. $l = 1, 2, ...$ and $m = 0, \pm1, ...$ The only relevant modes for our calculation, though, are $l = 1, m = \pm1$

The Hamiltonian of the Spasing system is:

$$H = H_{sp} + H_{gain} + H_{int} \tag{5.23}$$

H_{sp} is the Hamiltonian of the surface plasmons themselves:

$$H_{sp} = \hbar\omega_{sp}\sum_{m=\pm1}\hat{a}_m^*\hat{a}_m \tag{5.24}$$

$\hat{a}_m^*$ and $\hat{a}_m$ are the creation and annihilation operators. In this case, the surface plasmons (SPs), including the creation and annihilation operators, can be treated as quasi-classical quantities $a_n = a_{0n}e^{-i\omega t}$ With a_{0n} as a slowly varying amplitude. This allows us to classify the number of plasmons per mode at a given time as $N_p = |a_{0n}|^2$.

H_{gain} is the Hamiltonian of the TMDC monolayer defined with our semi-classical, two-band model. H_{int} is the Hamiltonian of the TMDC monolayer interacting with the Electric field of the silver nanospheroid created by the incident pulse:

$$H_{int} = -\nu_{\mathbf{K}} \sum_{\mathscr{K}=\mathbf{K},\mathbf{K}'} \int \sum_{m=\pm 1} \mathbf{F}_m(\mathbf{r})\hat{\mathbf{d}}_{\mathscr{K}}(\mathbf{r})d^2\mathbf{r} \tag{5.25}$$

$\hat{\mathbf{d}}_{\mathscr{K}}$ is the inter-band dipole matrix element from Equation 7, but for the K and K' valleys. $\mathbf{D}_{cv}(\mathscr{K}) = e\langle \Psi^c_{\mathscr{K}}| i\frac{\partial}{\partial \mathscr{K}} |\Psi^v_{\mathscr{K}}\rangle$. The electric field operator is:

$$F_m(\mathbf{r},t) = -A_{sp}\nabla\phi_m(\mathbf{r})(\hat{a}_m e^{-i\omega_{sp}t} + \hat{a}^*_m e^{i\omega_{sp}t}) \tag{5.26}$$

Where:

$$A_{sp} = \sqrt{\frac{4\pi\hbar s_n}{\epsilon_d s'_n}} \tag{5.27}$$

$$s'_n = \frac{dRe[s(\omega)]}{d\omega}\Big|_{\omega=\omega_{sp}} \tag{5.28}$$

The primary equations of the spasing system describe its dynamics quasi-classically using the approximation mentioned earlier for treating the spasers classically, yet also treating the TMDC quantum mechanically within the density matrix approach. These equations were derived by Stockman in 2010 using the Heisenberg equation of motion and the Rotating Wave Approximation.(5)

$$\dot{a}_m = \quad [i(\omega - \omega_{sp}) - \gamma_{sp}]a_m \tag{5.29}$$

$$+i\nu_{\mathscr{K}} \int \sum_{\mathscr{K}} \rho^*_{\mathscr{K}}(\mathbf{r})\tilde{\Omega}^*_{m,\mathscr{K}}(\mathbf{r})d^2\mathbf{r}$$

$$\dot{n}_{\mathcal{K}}(\mathbf{r}) = \quad -4 \sum_{m=\pm 1} Im[\rho_{\mathcal{K}} \tilde{\Omega}_{m,\mathcal{K}}(\mathbf{r}) a_m] \tag{5.30}$$

$$-\gamma_{2\mathcal{K}}(\mathbf{r})[1 + n_{\mathcal{K}}(\mathbf{r})]$$

$$\dot{\rho}_{\mathcal{K}}(\mathbf{r}) = \quad [-i(\omega - \omega_{21}) - \Gamma_{12}]\rho_{\mathcal{K}}(\mathbf{r}) \tag{5.31}$$

$$+in_{\mathcal{K}}(\mathbf{r}) \sum_{\mathcal{K}} \tilde{\Omega}^*_{m,\mathcal{K}}(\mathbf{r}) \hat{a}^*_m$$

$\tilde{\Omega}_{m,\mathcal{K}}(\mathbf{r})$ is the Rabi frequency defined as:

$$\tilde{\Omega}_{m,\mathcal{K}}(\mathbf{r}) = -\frac{1}{\hbar} A_{sp} \nabla \phi_m(\mathbf{r}) \hat{\mathbf{d}}_{\mathcal{K}}(\mathbf{r}) \tag{5.32}$$

And $\gamma_{2\mathcal{K}}(\mathbf{r})$ is the spontaneous emission rate of SPs:

$$\gamma_{2\mathcal{K}}(\mathbf{r}) = \frac{2(\gamma_{sp} + \Gamma_{12})}{(\omega_{sp} - \omega_{21})^2 + (\gamma_{sp} + \Gamma_{12})^2} \sum_{m=\pm 1} |\tilde{\Omega}_{m,\mathcal{K}}(\mathbf{r})|^2 \tag{5.33}$$

The population inversion, $n_{\mathcal{K}}(\mathbf{r})$ is the main connection between the Stockman equations and conduction band populations derived by Motlagh. We define $n(\mathbf{r}) \equiv N_c(\mathbf{q}, t) = |\beta_{c\mathbf{q}}(t)|^2$.

5.2.3 Parameters and Initial Conditions

The silver nanospheroid has a semimajor axis of 12nm and a semiminor axis of 1nm in height, while the TMDC flake is circular with a 14nm radius. Both materials are suspended in a uniform dielectric medium with a constant $\epsilon_d = 1.6$. The band-gap of the TMDC flake, Δ_g, is 1.6 eV. The semiminor axis of the nanospheroid and the dielectric constant of the system's medium has been chosen to ensure the SP frequency ω_{sp} matches the dipole transition frequency $\omega_{21} = \frac{\Delta_g}{\hbar}$ of the
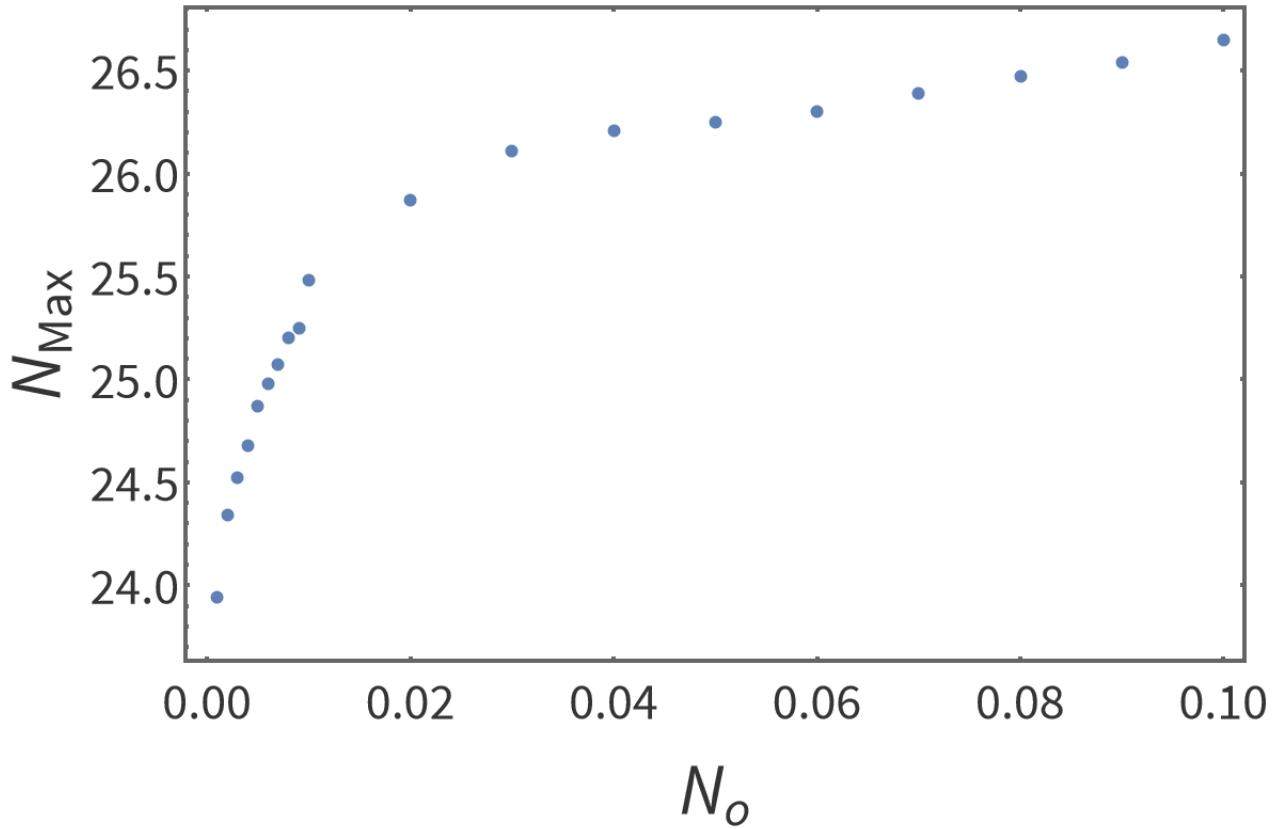
Figure 5.3 We simulated the spasing system with varying initial conditions to maximize plasmon generation. Here, the $N_m(max)$ is the total number of plasmons at the peak of the spaser pulse, and $N_m(int)$ is the initial number of plasmons injected into the system. The incoming pulse in this situation was coupled to the $m = 1$ mode, so the injected plasmons and maximum plasmons are all from the same mode. The nonlinear dependence for lower numbers of plasmons arises from the two parts of Eqn (17). For a higher number of injected plasmons, the first part of the equation is linear and dominant; however, for lower numbers of plasmons, the second nonlinear part of the equation becomes dominant.

TMDC material. This ensures a proper transfer of energy into the spasing modes. The coherent relaxation rate for the TMDC layer is $\Gamma_{12} = 1.51ps^{-1}$, and the plasmon relaxation rate for the spheroid is $\gamma_{sp} = 15ps^{-1}$.

We set the initial number of plasmons in the system to 0. Figure 2 shows an interesting nonlinear dependence the maximum number of plasmons in a mode has on the initial number of plasmons "injected" into that mode. This is a product of the Stockman equations for $N_{int} > 1$, and the relationship is linear. The initial exciton populations also are related to the time at which the initial avalanche occurs. Such an effect was documented by Stockman in Ref(5)when we investigated the effect of initial plasmons in the system. Stockman discovered that systems with a higher amount of initial plasmons experienced a decay into the spasing mode a few picoseconds sooner than those with lower populations. This effect can be seen in Fig. 4 (A-C) in the case of larger exciton populations. This happens earlier with a larger population due to the probabilistic nature of stimulated emission and higher populations occupying higher energy levels.

5.3 Results

For simulating the pulse generating excited populations in TMDC, we tested five different strengths of fields: $F = 0.1 - 0.7V\mathring{A}^{-1}$. The field strengths could be relatively low for this purpose because of how few plasmons are needed to achieve spasing, $N \leq 100$. Once enough excitons are generated, a stimulated emission effect occurs, and the excitons quickly decay and generate plasmons in the metal. The needed population to achieve stimulated emission is 0.6 or sixty percent populated. However, the silver nanospheroid hinders this by screening the incoming field and creating a nonuniform distribution of K or K' valley populations in the TMDC layer. The valleys closer to the nanospheroid's center are significantly less populated than those near the edges. In addition,

Figure 5.4 Density plot comparing the concentration of populated regions inside for the K (left) and K' (right) valleys inside the TMDC monolayer flake for an incident pulse of strength $F = 0.25 V \AA^{-1}$. In this plot you can see how population inversion is maintained, as only one valley type is populated.
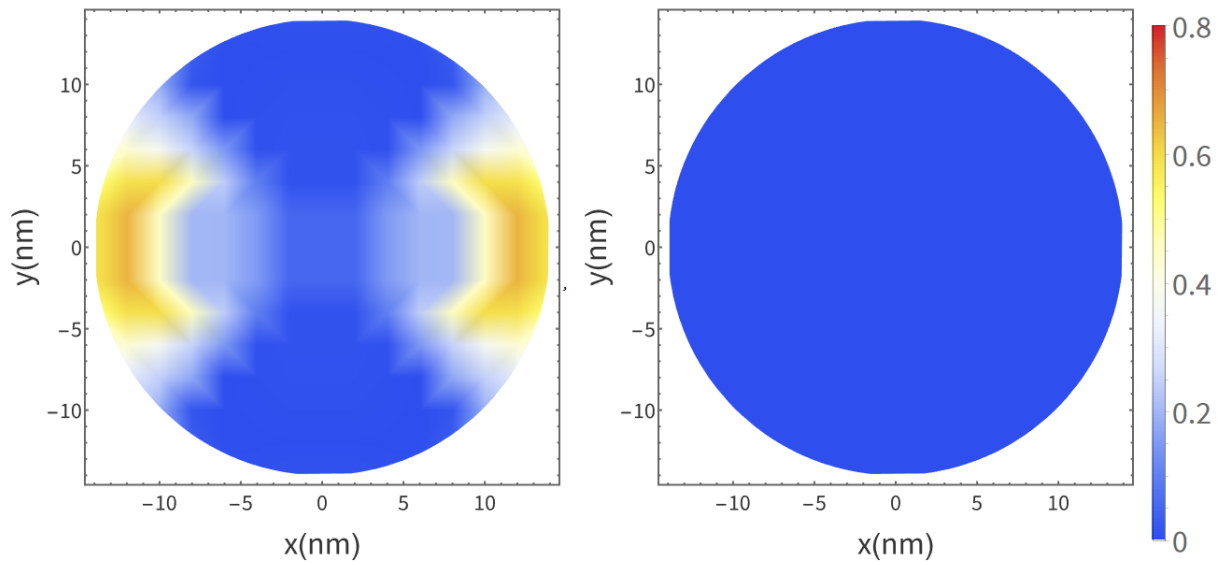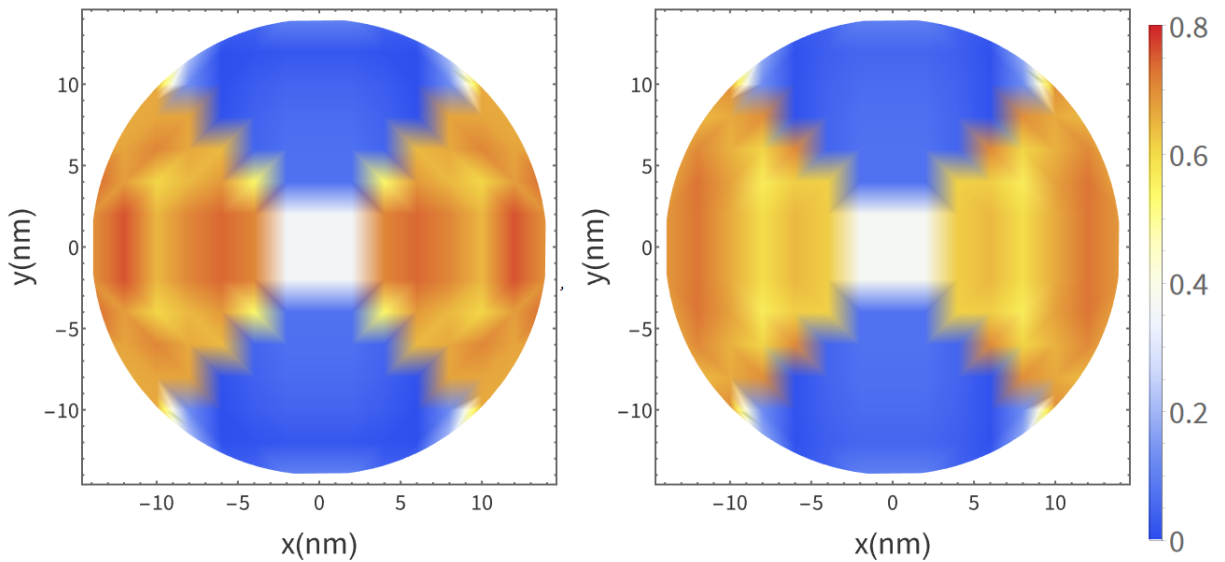

Figure 5.5 Density plot comparing the concentration of populated regions inside for the K (left) and K' (right) valleys inside the TMDC monolayer flake for an incident pulse of strength $F = 0.70 V \AA^{-1}$. In this plot you can see how population inversion is not maintained, as both valley types are populated.
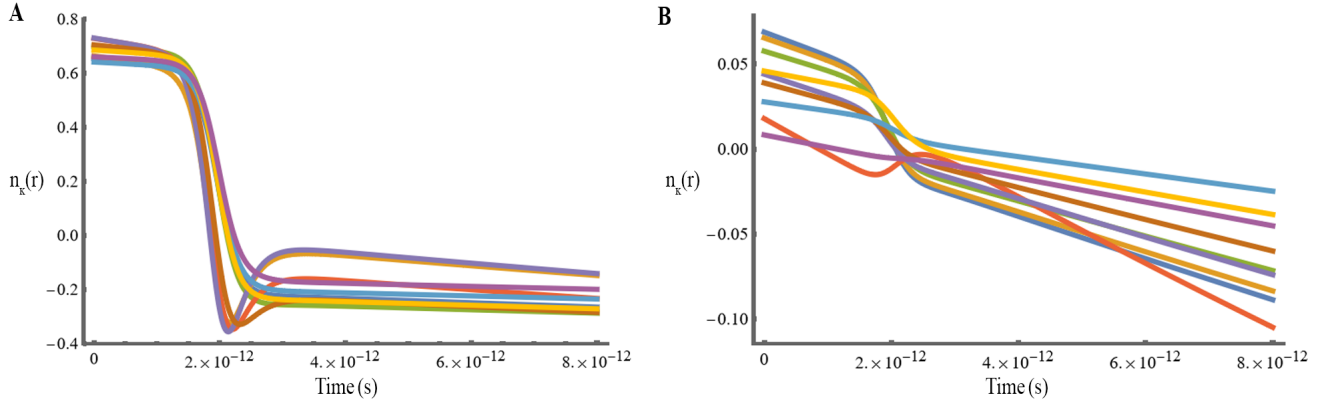
Figure 5.6 The avalanche effect of stimulated emission is shown in both Fig. 4.3(A) and Fig. 4.3(B), the x-axis is time in seconds, and the y-axis is conduction band population $n_c(r)$. Each line represents the population in a K valley located at a different position in the TMDC layer. The pulse strength was $F = 0.7V\mathring{A}^{-1}$ and coupled to the $m = 1$ mode. A) is the dynamics of the population in the K valleys located around the edge of the nanospheroid. These positions achieve higher populations and experience the avalanche effect simultaneously; however, not every position experiences the inherent feedback of the spaser similarly. B) shows the same simulated event but for positions closer to the nanospheroid's center. These populations experience few nonlinear effects and quickly decay. After the initial avalanche, the plasmons in A behave similarly to the plasmons in B.

the plasmon modes are coupled to the TMDC layer as a whole; therefore, if only a few areas of the TMDC layer are above sixty percent populated, then there still is not enough to generate a significant stimulated emission effect the plasmons slowly decay.

We used larger field strengths to overcome this effect; however, as shown in Ref(29) valley polarization decreases as the total population generated in the K and K' valleys increases. Field strengths of $F = 0.25 - 0.7V\mathring{A}^{-1}$ did achieve enough populations to reach stimulated emission. Stimulated emission in spasers manifests as a sudden transfer of energy from the exciton state of the gain medium to the plasmon state of the metal, as shown in Ref(5). Stockman referred to this as an "avalanche," In our nonuniform gain medium, this appears as multiple different locations

Figure 5.7 Here the number of plasmons are plotted with respect to time. The incident pulse strength is $F = 0.25V\,\mathring{A}^{-1}$ and populates only the K valleys in the TMDC. We can see in this plot that this effect causes only one plasmon mode to be stimulated as the competing mode stays nearly 0.
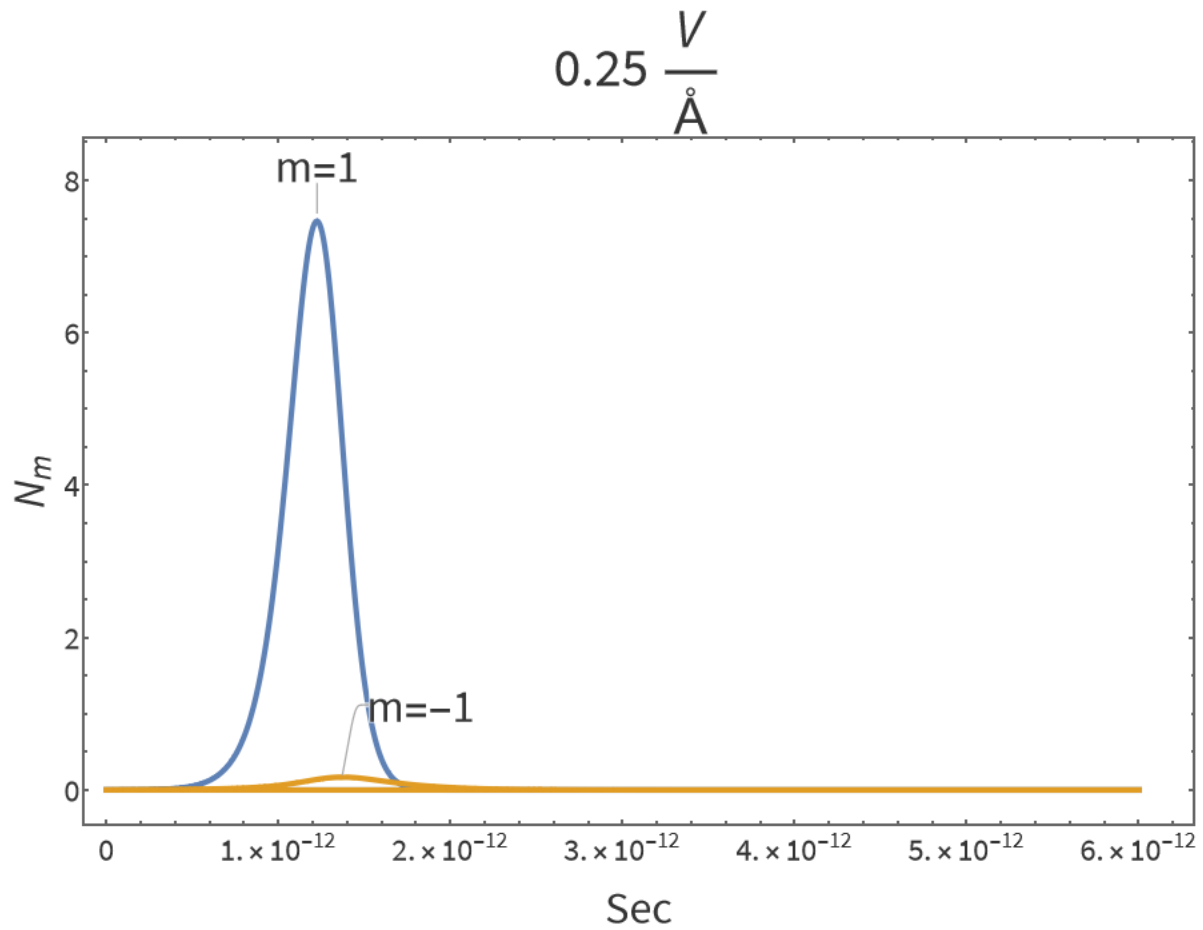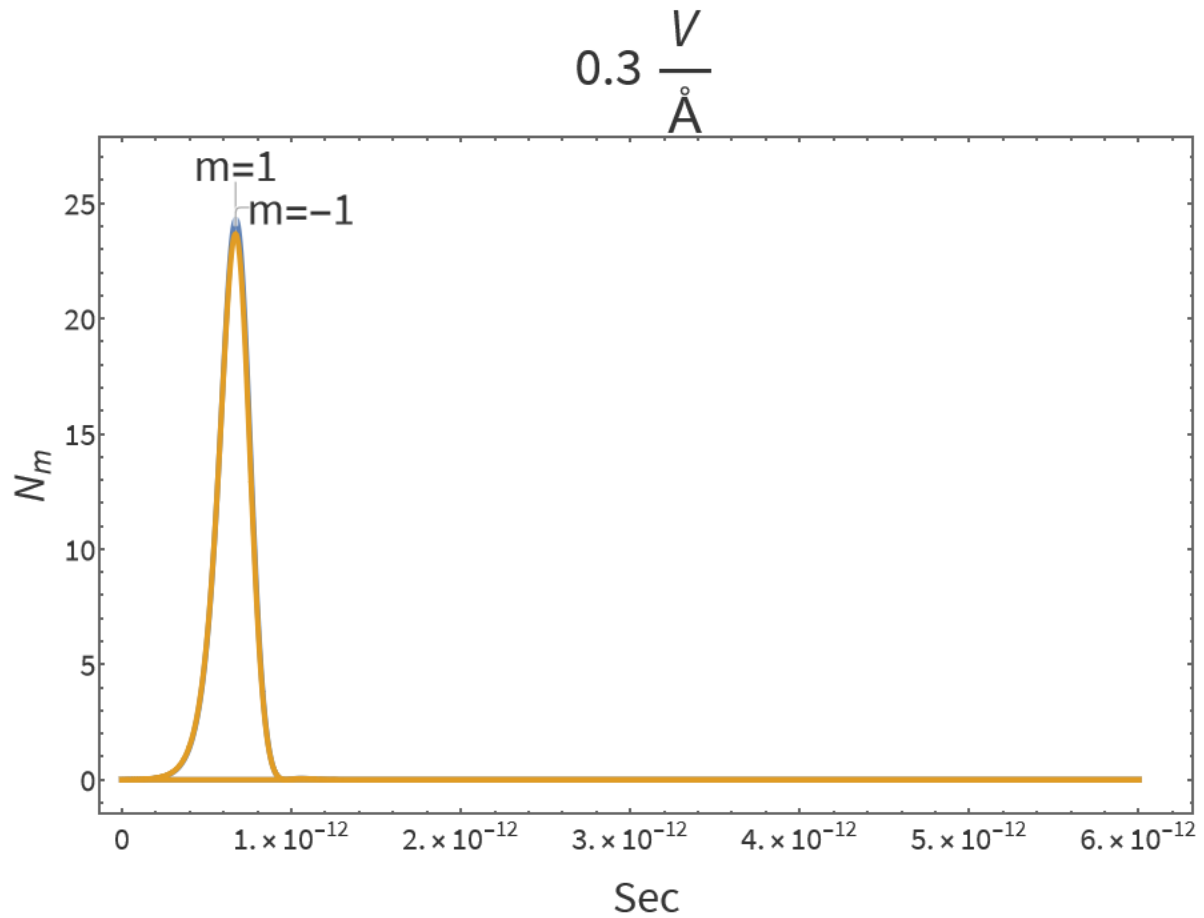
Figure 5.8 Here the number of plasmons are plotted with respect to time. The incident pulse strength is $F = 0.30 V \mathring{A}^{-1}$ and populates both the K and K' valleys in the TMDC. We can see in this plot that this effect causes both plasmon modes to be stimulated.

decaying at once. Fig. 5.6 (A) shows this avalanche. Fig. 5.6 (A) also shows some excitons returning to their excited states a few picoseconds after the avalanche. This is due to an inherent feedback mechanism in the spaser where excitons stimulating plasmons are just as likely as plasmons restimulating excitons. The feedback mechanism is not strong enough to create a second avalanche effect, as most plasmon energy is lost through radiation.

For a field strength of $F = 0.25 V \mathring{A}^{-1}$, our initial goal of a stimulated only one plasmon mode was achieved. This was the only field strength were this occurred, however. In Fig. 5.4, we can see that only the K valleys were populated and in Fig 5.7, we can see that only one plasmon mode was stimulated even though it quickly decayed. Therefore, for our specific parameters, $F = 0.25 V \mathring{A}^{-1}$ exists as a "sweet spot" in which a circularly polarized pulse can stimulate a select plasmon mode and become amplified as an elliptically polarized pulse as shown in Fig 5.9.

Fig. 5.8 shows the generation of plasmons with high field strengths. Most notably, both modes are generated nearly equally in all higher cases as well as valley polarization decreases. The feedback mechanism is very selective even when valley polarization decreases. When we run the calculation with a hypothetical uniform population in one mode, we find that both plasmon modes are still generated initially. For example, if the K valley conduction band is pumped from a single pulse to sixty percent and the K' conduction band population remains zero, both the $m = 1$ and $m = -1$ modes will accumulate plasmons as exciton decay in the K valley stimulates plasmon creation in both. A uniform, hypothetical K valley conduction band populates both valleys because of the Rabi frequency's dipole nature at our given radius of TMDC flake which determines the feedback mechanism's behavior. The feedback mechanism is the most critical aspect of the topological spaser. Since the initial avalanche into the plasmon modes is unselective in our case, it is a poor method to generate controllable modes for purposes in ultra-fast information processing. After

this, however, the Rabi frequencies are strongly coupled to the K or K' valley, and each plasmon mode only transfers its energy into its coupled valley. A mathematical description of the valley to mode coupling can be found in Ref(36).

The critical challenge for the type II topological spaser is how to better control the stimulation of one mode over the other. This might be achieved by manipulating system parameters even when the initial valley polarization is low, and the Rabi frequency is coupled to both modes. As shown above, in this chapter, the peak number of plasmons in a mode depends on several initial conditions. For example, more initial plasmons in a specific mode or initial exciton populations in a particular valley. These conditions will create two unequal peaks of plasmons, with one mode containing a higher number than the other. The larger the separation between the initial conditions of both modes, the greater the separation in the resultant plasmon peaks. This critical feature defines whether the topological spaser is selective or not. Suppose one plasmon mode reaches a higher peak amount of plasmons than the other after the initial exciton-plasmon cycle. In that case, it is more likely that those plasmons, coupled to a specific valley in the TMDC, generate a large enough electric field to stimulate exciton generation in one valley instead of the other. This causes only one valley to reach the threshold value for the avalanche effect and creates a second situation that mirrors the initial conditions where one exciton valley is more populated than the other. One mode has more initial plasmons than the other for the second cycle. The second cycle has a lower number of plasmons than the first because the plasmons that populated the opposite valley failed to create enough excitons to reach the necessary threshold for stimulated emission. Thus, the excitons slowly decayed individually. So, the second mode acts as a loss for the other mode. This is the "competition" between modes as described in previous literature. For the selective nature of the topological spaser to appear, the separation between the number of plasmons generated in

each mode would have to increase until the energy loss generated by one mode not reaching the threshold for the avalanche effect causes one mode to decay to zero before the other. This means that the last exciton-plasmon cycles are selective and generate only one resultant plasmon mode.

5.3.1 Far-Field Radiation

The derivation for the dipole moment of the far field radiation follows Ref(37). The spasing system is an oscillating electric dipole with two significant contributions: the silver nanospheroid and the TMDC layer.

$$\mathbf{d}_{total} = \mathbf{d}_{TMDC} + \mathbf{d}_{Metal} \tag{5.34}$$

The TMDC layer's contribution is described by the non-diagonal part of the density matrix of TMDC:

$$\mathbf{d}_{TMDC} = \sum_{\mathscr{K}=\mathbf{K},\mathbf{K'}} \rho_{\mathscr{K}} \mathbf{d}_{\mathscr{K}} e^{i\omega t} + \rho_{\mathscr{K}}^* \mathbf{d}_{\mathscr{K}}^* e^{-i\omega t} \tag{5.35}$$

While the contribution of the silver nanospheroid is determined by calculating the electric field inside the metal.

$$\mathbf{d}_{Metal} = \int_V \frac{Re[\epsilon_{metal} - \epsilon_d]}{4\pi} F_m(\mathbf{r}, t) d\mathbf{r} \tag{5.36}$$

The nanospheroid's contribution is directly proportional to the number of plasmons in each mode. Here we find that the Far-Field Radiation emitted by the Type II topological spaser is also affected by the lack of valley polarization in the TMDC monolayer. Our results are similar to when

the second regime of a spasing is when both modes are generated, and the expected polarization of the radiation is elliptical; however, the similar peaks of plasmon generation in Fig. 4, the radiation in each case in linearly polarized.

5.3.2 Conclusion

This chapter has more accurately described type II topological spasers' potential behavior and limitations. As a result, we can be confident that the system has two topologically protected modes equally capable of spasing. However, choosing which mode is stimulated is the key and the most difficult one to achieve. Future research could focus on pulse pumping different topological materials with properties that favor more oscillations between the plasmon modes and the excitons or a continuation of research into continuous pumping to ensure the feedback mechanism is permanently active.

Figure 5.9 Here the Electric Field components of the resultant far field radiation are plotted with respect to time. The incident pulse strength is $F = 0.25V\mathring{A}^{-1}$ and populates only the K valleys in the TMDC. We can see in this plot that this effect causes only one plasmon mode to be stimulated as the competing mode stays nearly 0 in Fig 5.7. This results in the incoming circularly polarized pulse being transformed into an elliptically polarized one.
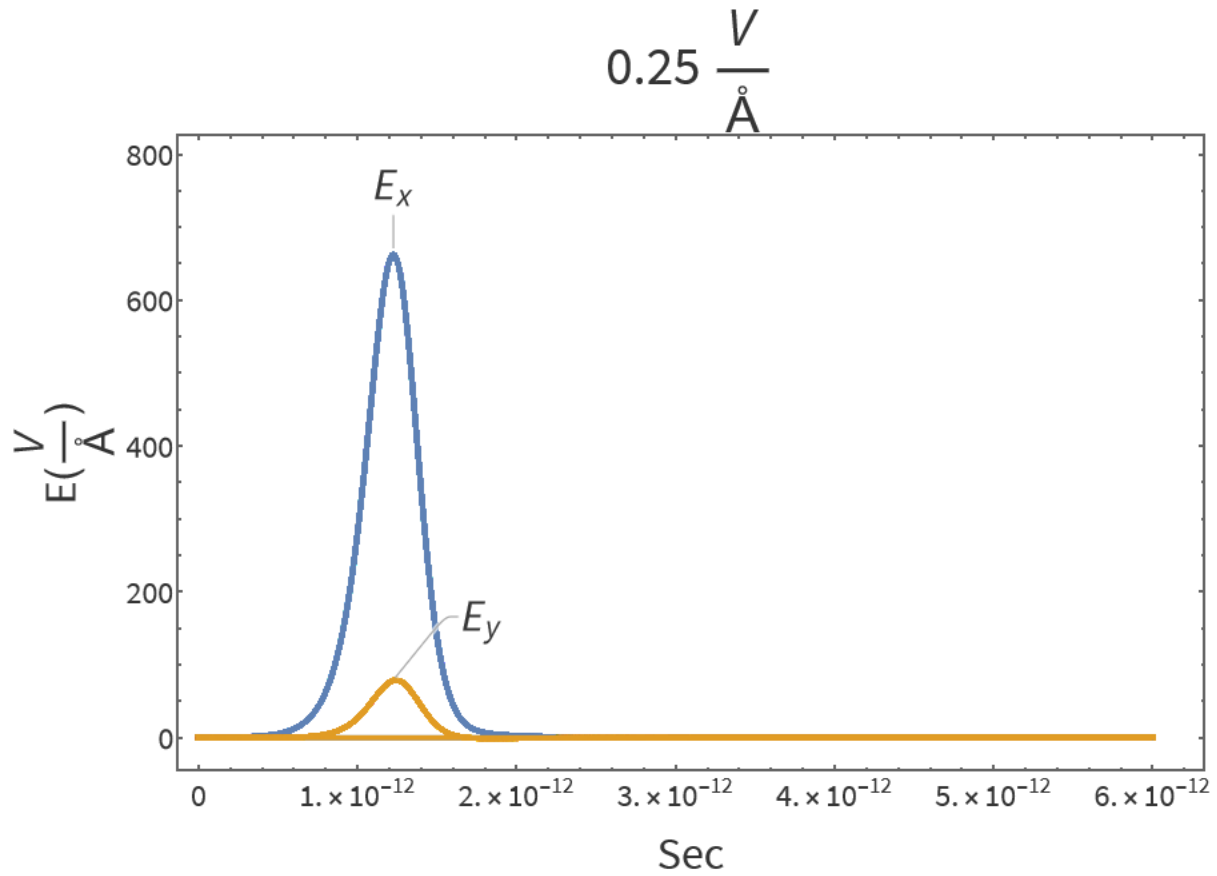
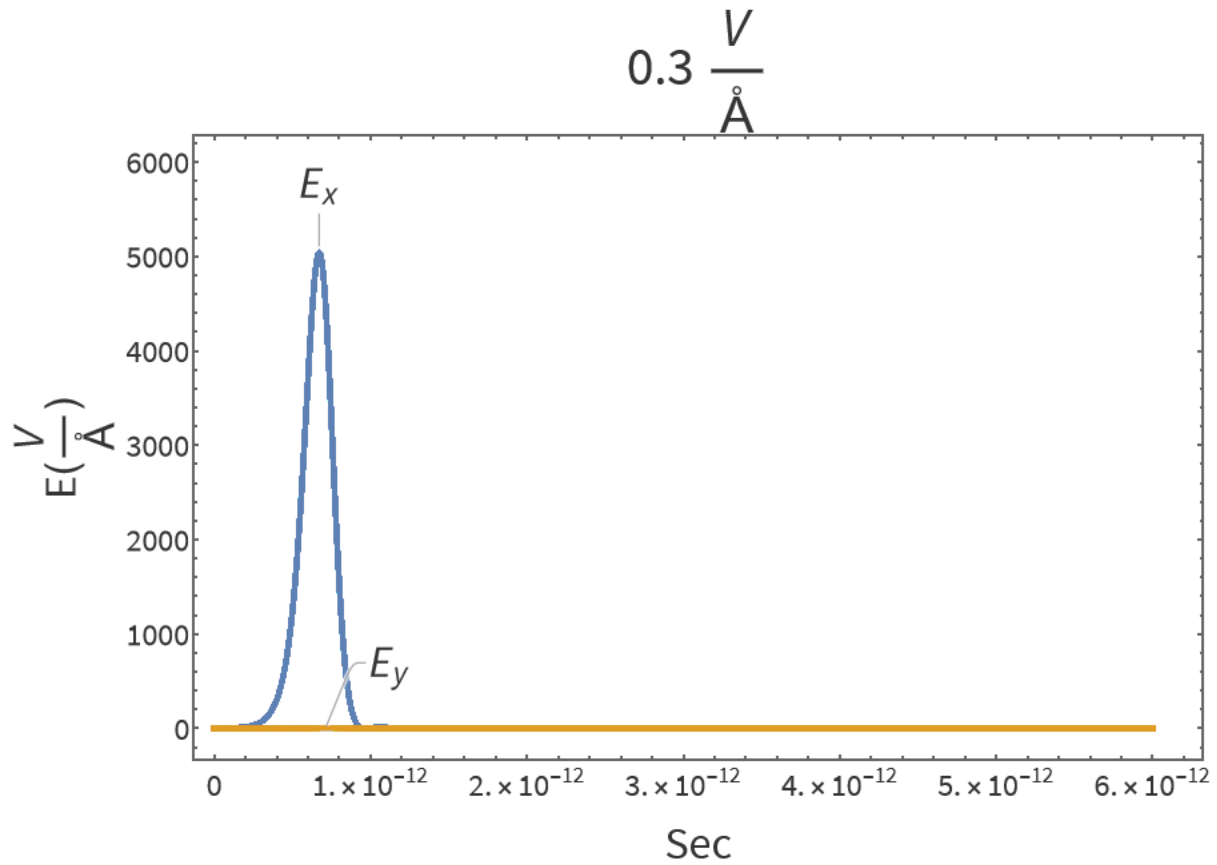Figure 5.10 Here the Electric Field components of the resultant far field radiation are plotted with respect to time. The incident pulse strength is $F = 0.30V\mathring{A}^{-1}$ and populates both the K and K' valleys in the TMDC. We can see in this plot that this effect causes both plasmon modes to be stimulated in Fig 5.8. This results in the incoming circularly polarized pulse being transformed into a linear polarized one.

CHAPTER 6

CONCLUSION

In conclusion, we have demonstrated that Chiral Berry Plasmons can be effectively tuned by changes in their environment and the Fermi level and bandgap of the material. This suggests the potential for new and exciting applications in plasmonics and photonics. The topological nanospaser is an emerging area of research with great potential for practical applications, and our work has contributed to the understanding of the underlying physics of these systems. Future directions for topological nanospaser research include investigating alternative materials to MoS2 as potential gain media and exploring new ways to generate enough excitons for plasmons to form a spaser, which is currently a challenge in the field. One possible solution could be to apply the three-level spaser equations derived in Chapter 4 to the topological spaser in Chapter 5. Additionally, further research could address higher pumping pulse strengths and the lack of valley polarization in the topological spaser. Our findings pave the way for future investigations and advancements in topological nanospasers and Chiral Berry Plasmons. The ability to tune these plasmons effectively is a significant step forward in the field, and we are excited to see where this research will lead.

REFERENCES

[1] Resonant Raman-Brillouin scattering in semiconductor and metallic nanostructures: from nano-acoustics to acousto-plasmonics. Technical report.

[2] Stefan A. Maier. *Plasmonics : fundamentals and applications*. Springer, 2007.

[3] Di Xiao, Ming Che Chang, and Qian Niu. Berry phase effects on electronic properties. *Reviews of Modern Physics*, 82(3), 2010.

[4] Ruitao Lv, Humberto Terrones, Ana Laura Elías, Néstor Perea-López, Humberto R. Gutiérrez, Eduardo Cruz-Silva, Lakshmy Pulickal Rajukumar, Mildred S. Dresselhaus, and Mauricio Terrones. Two-dimensional transition metal dichalcogenides: Clusters, ribbons, sheets and more, 2015.

[5] Mark I Stockman. The spaser as a nanoscale quantum generator and ultrafast amplifier. *Journal of Optics A: Pure and Applied Optics*, 12(2), 2010.

[6] David Pines and David Bohm. A collective description of electron interactions: II. Collective vs individual particle aspects of the interactions. *Physical Review*, 85(2), 1952.

[7] Mark I Stockman. Brief history of spaser from conception to the future, 2020.

[8] Ekaterina I Galanzha, Robert Weingold, Dmitry A Nedosekin, Mustafa Sarimollaoglu, Jacqueline Nolan, Walter Harrington, Alexander S Kuchyanov, Roman G Parkhomenko, Fumiya Watanabe, Zeid Nima, Alexandru S Biris, Alexander I Plekhanov, Mark I Stockman, and Vladimir P Zharov. Spaser as a biological probe. *Nature Communications*, 8, 2017.

[9] Anshuman Kumar, Andrei Nemilentsau, Kin Hung Fung, George Hanson, Nicholas X. Fang, and Tony Low. Chiral plasmon in gapped Dirac systems. *Physical Review B*, 93(4), 1 2016.

[10] Mark S Rudner. Chiral Berry Plasmons in a Disk. Technical report, 2017.

[11] Ren Min Ma, Rupert F. Oulton, Volker J. Sorger, and Xiang Zhang. Plasmon lasers: Coherent light source at molecular scales, 2013.

[12] Mark I Stockman. Nanoplasmonic sensing and detection. *Science*, 348(6232), 2015.

[13] Justin C W Song and Mark S Rudner. Chiral plasmons without magnetic field. *Proceedings of the National Academy of Sciences of the United States of America*, 113(17), 2016.

[14] W L Mochán. Plasmons. *Reference Module in Materials Science and Materials Engineering*, 11 2016.

[15] David J. Griffiths and Colin Inglefield. Introduction to Electrodynamics . *American Journal of Physics*, 73(6), 2005.

[16] John David Jackson. *Classical Electrodynamics-Third Edition*. 1998.

[17] Di Xiao, Ming Che Chang, and Qian Niu. Berry phase effects on electronic properties. *Reviews of Modern Physics*, 82(3):1959–2007, 7 2010.

[18] Arno Bohm, Ali Mostafazadeh, Hiroyasu Koizumi, Qian Niu, and Joseph Zwanziger. *The Geometric Phase in Quantum Systems*. 2003.

[19] Barry Simon. Holonomy, the quantum adiabatic theorem, and Berry's phase. *Physical Review Letters*, 51(24), 1983.

[20] David J. Griffiths and Darrell F. Schroeter. *Introduction to Quantum Mechanics*. 2018.

[21] J. J. Sakurai and Jim Napolitano. *Modern Quantum Mechanics*. 2017.

[22] Berry Michael. Quantal phase factors accompanying adiabatic changes. Technical report, 1984.

[23] Kin Fai Mak, Changgu Lee, James Hone, Jie Shan, and Tony F. Heinz. Atomically thin MoS2: A new direct-gap semiconductor. *Physical Review Letters*, 105(13), 2010.

[24] Manish Chhowalla, Hyeon Suk Shin, Goki Eda, Lain Jong Li, Kian Ping Loh, and Hua Zhang.

The chemistry of two-dimensional layered transition metal dichalcogenide nanosheets, 2013.

[25] D B Mast, A J Dahm, and A L Fetter. Observation of bulk and edge magnetoplasmons in a two-dimensional electron fluid. *Physical Review Letters*, 54(15), 1985.

[26] Alexander L Fetter. Edge magnetoplasmons in a bounded two-dimensional electron fluid. *Physical Review B*, 32(12), 1985.

[27] Diabolical points in the spectra of triangles. *Proceedings of the Royal Society of London. A. Mathematical and Physical Sciences*, 392(1802), 1984.

[28] Dafei Jin, Ling Lu, Zhong Wang, Chen Fang, John D Joannopoulos, Marin Soljačić, Liang Fu, and Nicholas X Fang. Topological magnetoplasmon. *Nature Communications*, 7, 2016.

[29] S Azar Oliaei Motlagh, Jhih Sheng Wu, Vadym Apalkov, and Mark I Stockman. Femtosecond valley polarization and topological resonances in transition metal dichalcogenides. *Physical Review B*, 98(8), 2018.

[30] David J Bergman and Mark I Stockman. Surface Plasmon Amplification by Stimulated Emission of Radiation: Quantum Generation of Coherent Surface Plasmons in Nanosystems. *Physical Review Letters*, 90(2), 2003.

[31] Mark I Stockman. Spasers explained, 2008.

[32] Lukas Novotny and Stephan J Stranick. Near-field optical microscopy and spectroscopy with pointed probes. In *Annual Review of Physical Chemistry*, volume 57, 2006.

[33] Lukas Novotny and Bert Hecht. *Principles of nano-optics*, volume 9781107005464. 2009.

[34] Timothy W Johnson, Zachary J Lapin, Ryan Beams, Nathan C Lindquist, Sergio G Rodrigo, Lukas Novotny, and Sang Hyun Oh. Highly reproducible near-field optical imaging with sub-20-nm resolution based on template-stripped gold pyramids. *ACS Nano*, 6(10), 2012.

[35] Mark I Stockman. Nanoplasmonics: past, present, and glimpse into future. *Optics Express*,

19(22), 2011.

[36] Rupesh Ghimire, Jhih Sheng Wu, Vadym Apalkov, and Mark I Stockman. Topological nanospaser. *Nanophotonics*, 9(4), 2020.

[37] Rupesh Ghimire, Fatemeh Nematollahi, Jhih Sheng Wu, Vadym Apalkov, and Mark I Stockman. TMDC-Based Topological Nanospaser: Single and Double Threshold Behavior. *ACS Photonics*, 8(3), 2021.

[38] Jhih Sheng Wu, Vadym Apalkov, and Mark I Stockman. Topological Spaser. *Physical Review Letters*, 124(1), 2020.

[39] L D LANDAU and E M LIFSHITZ. CHARGES IN ELECTROMAGNETIC FIELDS. In *Mechanics and Electrodynamics*. 1972.